6-1-2013

Metamaterial antennas for cognitive radio applications

Ahmed Rajaie Raslan

The American University in Cairo

School of Sciences and Engineering

Metamaterial Antennas for Cognitive Radio Applications

A Thesis Submitted to
The Electronics Engineering Department

in partial fulfillment of the requirements for
the degree of Master of Science

by Ahmed Rajaie Raslan

under the supervision of Dr. Amr Safwat and Dr. Ali Darwish

May / 2013

Approval Sheet Goes Here

To My Family

I present this thesis to you to express my deep gratitude and love

Thanks

ABSTRACT

Cognitive radio is one of the most promising techniques to efficiently utilize the radio frequency (RF) spectrum. As the Digital Video Broadcasting – Handheld (DVB-H) band is targeted $(470 - 862\ MHz)$, the size of the antenna becomes challenging.

Metamaterial concept is used as a miniaturization technique. Two antennas are designed, fabricated and measured. The first one achieved multiband operation by loading it with a metamaterial unit cell. These bands are controlled by engineering the dispersion relation of the unit cell.

The second one, which is a 2-lumped elements loaded antenna, achieved wideband operation through the entire DVB-H band with a planar size of $5 \times 2\ cm^2$. A model is proposed to explain, through simple numerical simulations and an optimization algorithm, the behavior of these component loaded antennas (which are equivalent to metamaterial inspired electrically small antennas).

ACKNOWLEDGMENT

I would like to express my deep appreciation for my supervisors, Dr. Amr Safwat and Dr. Ali Darwish for their endless support and help throughout this thesis.

I would also like to acknowledge the help I had received from my friend in the Microwave Lab., Eng. Amr A. Ibrahim. Finally, I would like to thank Eng. Ola Galal for her help in wielding the lumped inductors.

Contents

List of Figures

List of Tables

Chapter 1
Introduction

The need for higher data rates is increasing as a result of the transition from voice-only communications to multimedia type applications. The current static frequency allocation has led to a shortage in the radio frequency (RF) spectrum, and hence, the need of dynamic spectrum access (DSA) became a must. Cognitive radio (CR) is considered one of the most promising and innovative DSA techniques due to its two unique properties: cognitive capability and reconfigurability (as will be shown in chapter 2). Lots of research have been done on CR. As it has not been standardized yet, different research groups target different frequency bands.

1.1 Motivation and Objective of the Thesis

In Egypt, there is an approach to replace the analog TV with digital one. Thus, National Telecommunication Regulatory Authority (NTRA) supported a project to implement CR in the Digital Video Broadcasting-Handheld (DVB-H) band $(470 - 862\ MHz)$.

This thesis targets only the antenna implementation part of this project. The fact that this CR system needs to be installed in portable devices leads to many challenges. The first fundamental one is the size of the antenna. This arises from the fact that the wavelength of the DVB-H band ($35 \sim 64$ cm) is comparable to the portable devices. The second challenge is the need to have an omnidirectional radiation pattern antenna. Thus, users can transmit and receive data independently of their orientation. Finally, this antenna should have high efficiency because portable devices work with rechargeable batteries.

Metamaterial concept will be used to meet these requirements, especially the first one. The Greek word "meta" (means "beyond") is used to describe artificial materials with unique properties that do not exist in nature. Although, this concept had been proved mathematically in 1960s, the first verification experiment was done in 2001.

1.2 Thesis Organization

The thesis is organized as follows:

Chapter 2 outlines the importance of DSA techniques with focus on CR systems. A survey on different techniques used to implement different CR antennas is conducted.

Chapter 3 provides a brief background on the theory of 1-D metamaterial (metamaterial transmission lines). As an application, a multiband metamaterial antenna is designed, fabricated and measured.

Chapter 4 builds upon the concept in Chapter 3 by providing an approach to design a compact size antenna using metamaterial. This approach is called metamaterial inspired electrically small antennas. The chapter also addresses the progress that has been done in this approach in the past few years.

In Chapter 5, a model is proposed to design wideband electrically small antennas. A novel, compact size (electrically small), omnidirectional radiation pattern and high efficiency DVB-H antenna is designed, fabricated and tested.

Lastly, Chapter 7 concludes the thesis and states possible future work.

Chapter 2
Cognitive Radio

In this chapter, a brief introduction for Cognitive Radio (CR) is given. Concept, importance and different implementation approaches (from antenna point of view) are stated. Although the main objective of this thesis is to implement a CR antenna in the Digital Video Broadcasting - Handled (DVB-H) band ($470 - 862\ MHz$), the survey conducted here includes CR systems in higher band ($1 - 10\ GHz$) as well as the DVB-H band. Lastly, a summary for these techniques and the need to use metamaterial concept is provided (metamaterial itself will be discussed in the next chapter).

2.1 Introduction

The growth of communication systems and the need for higher data rates have led to a shortage in the radio frequency (RF) spectrum. One of the most important reasons for this shortage is the static frequency allocation which has caused a large portion of the spectrum to be underutilized. As a result, many dynamic spectrum access techniques have been developed to utilize the spectrum in a more efficient way.

Cognitive radio (CR) is one of the most promising solutions to exploit available spectrum efficiently. It was termed by Joseph Mitola in 1991. He defined it as “The point in which wireless personal digital assistants (PDAs) and the related networks are sufficiently computationally intelligent about radio resources and related computer-to-computer communications to detect user communications needs as a function of use context and to provide radio resources and wireless services most appropriate to those needs”[1].

Another definition was stated by Federal Communications Commission (FCC) as “a radio that can change its transmitter parameters based on interaction with the environment in which it operates” [2]. Thus, CR differs from conventional radio by giving users cognitive capability and reconfigurability. Cognitive capability is the ability to sense the surrounding environment and gather information about transmission efficiency, bandwidth, power, modulation, etc. Reconfigurability refers to the ability to rapidly adapt transmission parameters according to the sensed information.

2.2 Dynamic Spectrum Access Techniques

Three solutions have been suggested by FCC to improve spectrum utilization: spectrum reallocation, spectrum leasing and spectrum sharing, as shown in Fig. 2.1 [3]. Spectrum reallocation is a long-term solution and resulted in the opening of the 700 MHz TV band for CR operation. Spectrum leasing is an off-line solution. It allows frequency licensees to sell their channels to third parties. The third solution, which is spectrum sharing, has attracted the attention of many research activities. It is often known as dynamic spectrum access (DSA), [4].

Unlike the current static spectrum access, DSA enables users to dynamically access the spectrum using three different models as shown in the third raw in Fig. 2.1. The open sharing model enables all users to simultaneously access the

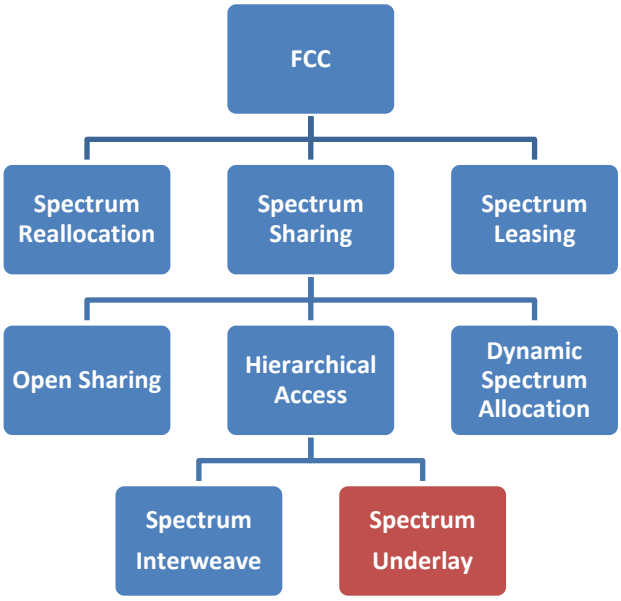

Figure 2.1: Solutions proposed by FCC to the spectrum underutilization problem. The spectrum underlay is the main focus of this thesis.

spectrum with certain constraints on the transmitted power according to the used protocol. WiFi and Bluetooth are examples for this model. The dynamic spectrum allocation improves the spectrum efficiency in a certain region for a specific time by assigning frequency band dynamically to wireless services according to their spatial and temporal traffic statistics.

The hierarchical model, which is the main concern of this chapter, enables the secondary user to access the spectrum bands that are not fully utilized by the primary user[1]. The only constraint in this model is that the quality of service

[1] Users sharing certain spectrum are divided into two categories, primary and secondary. Primary user has a spectrum license for certain region (assigned by FCC on long-term). Secondary user does not have a spectrum license, yet, he is allowed to temporally use the spectrum as long as QoS of the primary user is not affected.

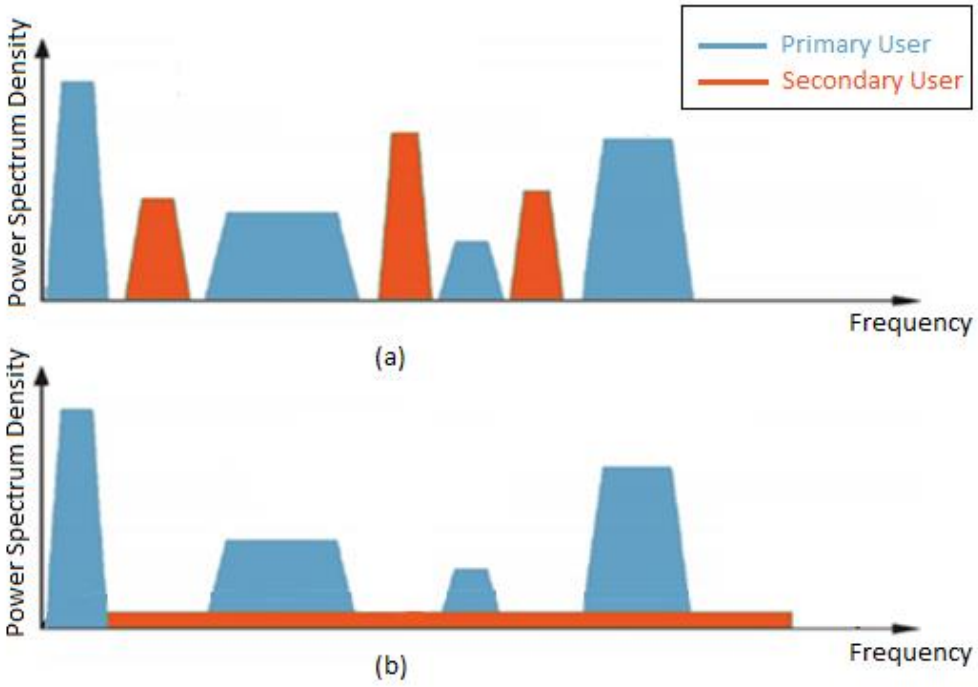

Figure 2.2: CR systems: (a) Spectrum Interweave (a), and (b) Spectrum Underlay [4].

(QoS) of the primary user is not affected. Two approaches are considered in this model: spectrum interweave and spectrum underlay.

In the spectrum interweave approach, the secondary user avoids the primary user using spectrum sensing and adaptive allocation techniques, as shown in Fig. 2.2 (a). This approach relies on the detection and exploitation of spectrum holes[2]. On the other hand, in the spectrum underlay approach, the secondary user operates under the noise floor of the primary user, as shown in Fig. 2.2 (b). An example of this approach is the ultra-wide band (UWB) transmission[3], in which the transmitted signal of the secondary user is spread over an ultra-wide frequency

[2] Spectrum holes: the part of the spectrum that is not used by the primary user (also known as spectrum white spaces)

[3] According to FCC, the antenna is defined to be UWB if its bandwidth exceeds the lesser of $500\ MHz$ or 20% of the center frequency. Since DVB-H has a bandwidth of 59% of the center frequency, UWB antenna is needed.

band. This UWB transmission enables very short distance, high speed and low power communication. This approach does not depend on the detection of the spectrum holes.

From antenna point of view, the spectrum interweave approach requires two antennas, sensing and reconfigurable, while the spectrum underlay approach requires only an UWB antenna. In the next sections, examples for different techniques used to implement these systems will be discussed. It should be noted that CR has not been standardized yet, and hence, different frequency bands are targeted by different research groups. In this work, although we target the DVB-H band $(470 - 862\ MHz)$, the survey is done on different frequency bands to have a better view for different implementation techniques.

2.3 Spectrum Interweave CR

In the spectrum Interweave CR, two types of antennas are needed, sensing and reconfigurable antennas. The sensing antenna, which is an UWB antenna, is used to sense the spectrum and find the spectrum holes. Using these data, the reconfigurable antenna is tuned to transmit at the frequencies of these holes. Many challenges concerning antenna design exist in this type of CR. The first challenge is the need to minimize the area containing both antennas. The coupling between the two antennas is an important factor in such a system, and therefore, many isolation techniques should be considered to minimize the effect of the two antennas on each other. Both antennas should also acquire an omni-directional radiation pattern.

Many works have been published in the frequency band from 1 to 10 GHz. In these publications, a complete spectrum interweave CR system was implemented (both sensing and reconfigurable antennas on the same substrate). On the other

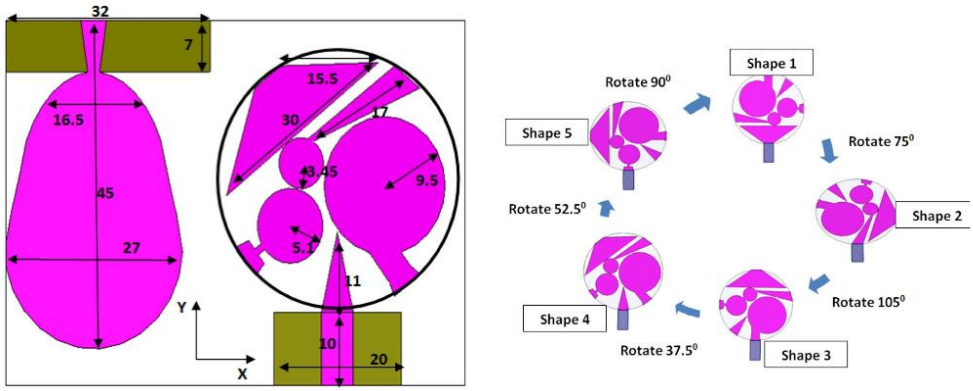

(a) **(b)**

Figure 2.3: (a) Sensing and reconfigurable antenna structures. (b) The five positions for the reconfigurable antenna.

hand, no work has been published in the DVB-H band. Therefore, research has been carried on both types of antennas alone.

2.3.1 Higher Frequency Band ($1-10\ GHz$)

CR systems consisting of sensing and reconfigurable antennas will be listed. These CR systems operate in the frequency band from $1-10$ GHz. This section serves as a survey for the most common techniques used to implement sensing and reconfigurable antennas on the same substrate.

2.3.1.1 Implementation of a Cognitive Radio Front-End Using Rotatable Controlled Reconfigurable Antennas

In [5], both sensing and frequency reconfigurable antennas were presented on the same substrate as shown in Fig. 2.3 (a). The sensing antenna was a modified egg-shaped monopole antenna and covered frequency band from $2-10\ GHz$. The frequency tunability was achieved by physically altering the patch shape. This was done by rotating a circular substrate section holding five different antenna patches using a stepper motor as shown in Fig. 2.3 (b). Using these five antennas,

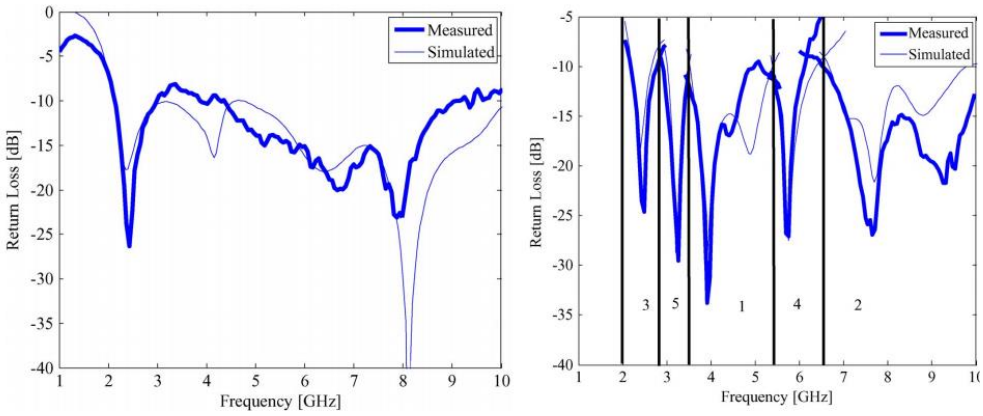

(a) **(b)**

Figure 2.4: Simulated and measured $|S_{11}|$ for (a) sensing antenna, and (b) reconfigurable antenna.

Figure 2.5: The fabricated antenna with the stepper motor mounted on the back of the substrate.

five bands could be achieved to cover the whole frequency range. Fig. 2.4 (a) and (b) shows simulated and measured $|S_{11}|$ for both antennas. Fig. 2.5 shows the fabricated antenna with the stepper motor mounted on the back of the substrate. Both sensing and reconfigurable antenna had an omnidirectional pattern with a planar structure of size $70 \times 50\ mm^2$.

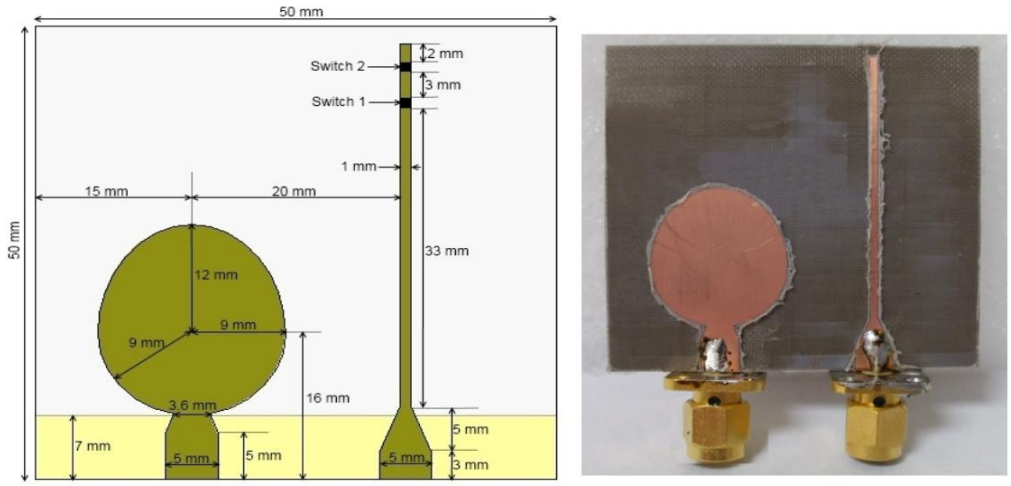

(a) **(b)**

Figure 2.6: (a) Structure of the sensing and reconfigurable antenna. (b) The fabricated antennas.

2.3.1.2 A Reconfigurable Cognitive Radio Antenna Design

In [6], a cognitive radio system composed of two microstrip line fed monopoles was implemented, as shown in Fig. 2.6. The sensing antenna was an egg-shaped monopole antenna and covered frequency band of $3.1 - 10.6\,GHz$, as shown in Fig. 2.7 (a). The reconfigurable antenna was a microstrip line loaded with two switches. This structure yielded three different resonances in the $3.1 - 10.6\,GHz$ frequency range, depending on the switches configuration. The measured resonance frequency corresponding to each configuration is shown in Fig. 2.7 (b). Both antennas had an omnidirectional radiation pattern with a planar structure of size $50 \times 50\,mm^2$.

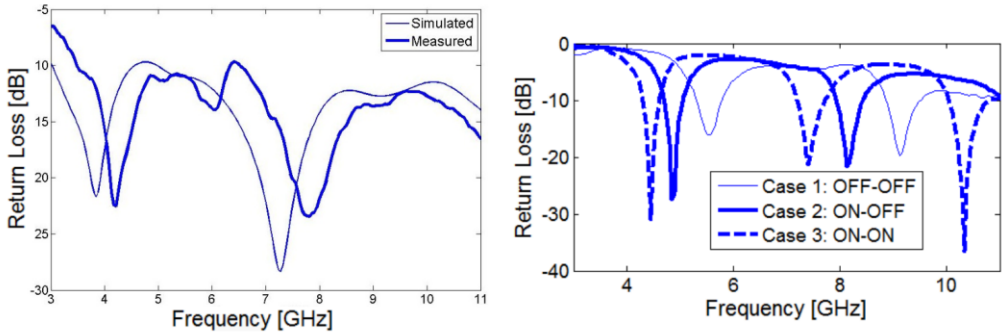

(a) **(b)**

Figure 2.7: (a) Simulated and measured $|S_{11}|$ for sensing antenna, and (b) measured $|S_{11}|$ reconfigurable antenna for different switches configuration.

2.3.1.3 Design and Implementation of an Integrated UWB/Reconfigurable-Slot Antenna for Cognitive Radio Applications

In [7], an incorporated planar UWB/reconfigurable-slot antenna was proposed for cognitive radio applications. Again, UWB antenna was implemented using the egg-shaped monopole antenna to cover the frequency range from $2-12\ GHz$. A slot resonator was precisely embedded in the disc monopole radiator to achieve an individual narrowband antenna as shown in Fig. 2.8. A varactor diode was inserted across the slot, providing a reconfigurable frequency function in the range of $5-6\ GHz$. By controlling the voltage across the varactor $(0-5\ V)$, the varactor capacitance achieved values between $7.643-0.469\ pF$. The slot was fed by an off-centered microstrip line that creates the desired matching across the tunable frequency band. The simulated and measured $|S_{11}|$ for both antennas are shown in Fig. 2.9 (a) and (b), respectively. Both antennas had an omnidirectional radiation pattern with a planar structure of size $40 \times 36\ mm^2$.

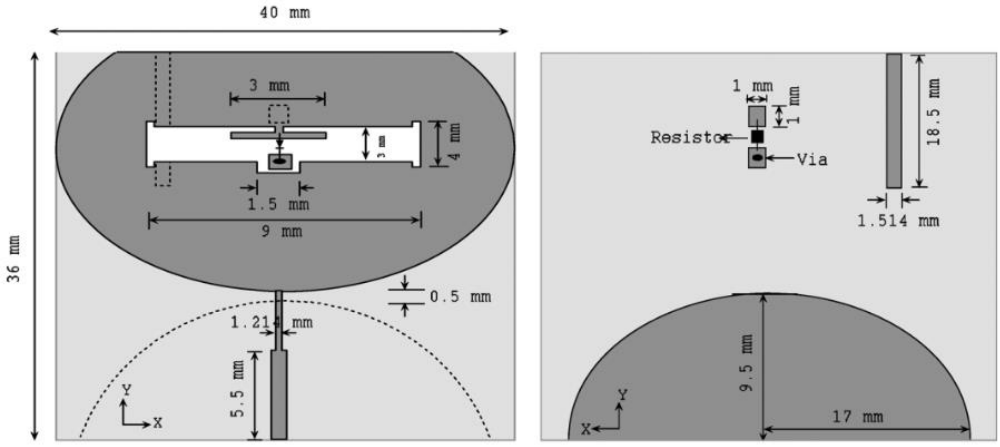

(a) **(b)**

Figure 2.8: Configuration of the antenna: (a) top view, and (b) bottom view.

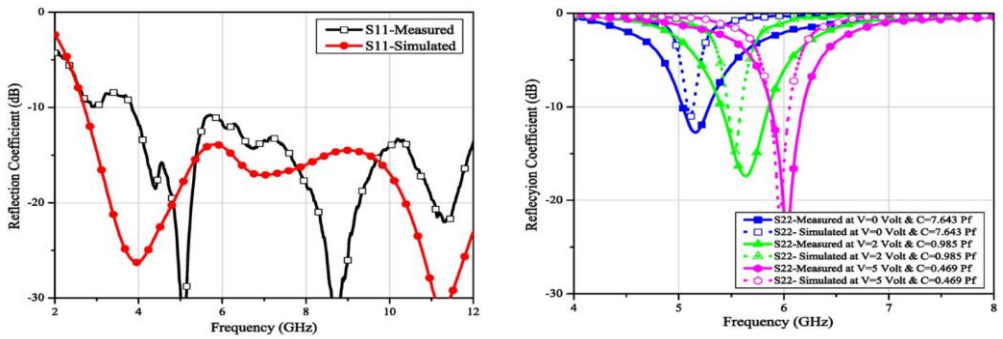

(a) **(b)**

Figure 2.9: (a) Simulated and measured $|S_{11}|$ for (a) sensing antenna, and (b) reconfigurable antenna.

2.3.1.4 A Comparison between Different Cognitive Radio Antenna Systems

In [8], both sensing and reconfigurable antenna were presented. The sensing antenna was an egg-shaped monopole antenna and covered the frequency band from $3 - 11\ GHz$. Reconfigurability was achieved by using two photoconductive

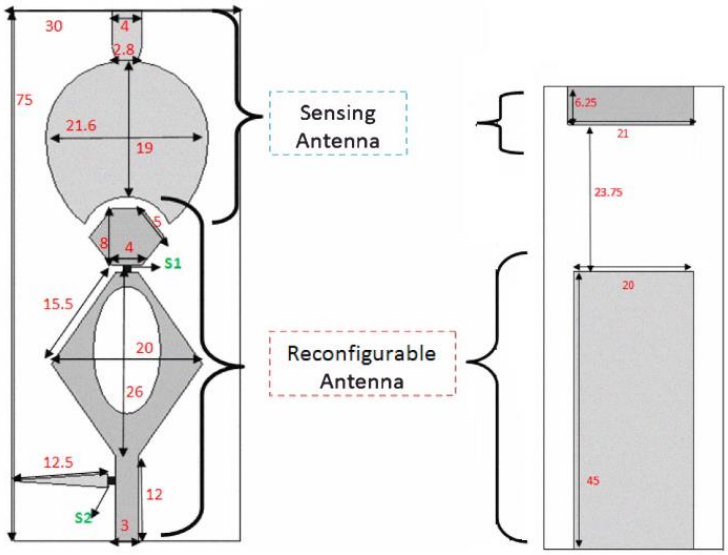

(a) **(b)**

Figure 2.10: Configuration of the antenna: (a) top view and (b) bottom view.

switches to connect different radiating parts. Three operating bands were achieved. Fig. 2.10 shows the structure of both antennas on the same substrate. These photoconductive switches were activated using laser diodes. Three different bands were achieved according to the switches configurations, as shown in Fig. 2.11. Both antennas had a planar structure of size $75 \times 30\ mm^2$.

2.3.2 DVB-H-Band

In these systems, the sensing antenna should be able to cover the frequency band from $470 - 862\ MHz$. Reconfigurable antenna, on the other hand, should be able to be tuned to cover the entire band with a channel bandwidth of $8\ MHz$ and $|S_{11}| - 6\ dB$ [9]. Different techniques have been used to design DVB-H sensing and reconfigurable antenna. In the following subsections, only reconfigurable antennas will be listed (as sensing antennas will be discussed in the spectrum

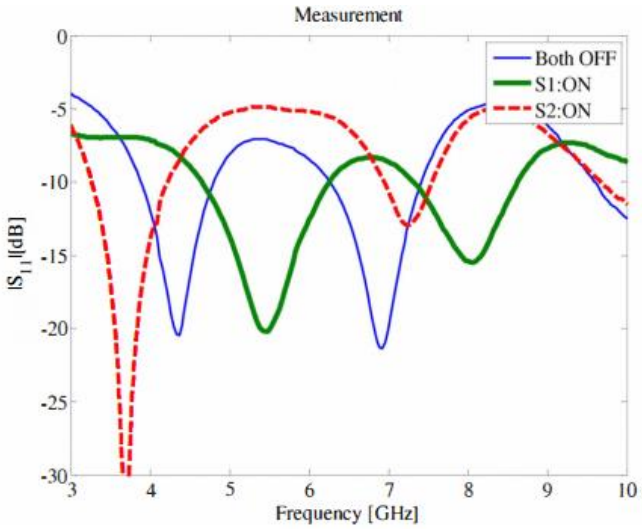

Figure 2.11: Measured $|S_{11}|$ for the reconfigurable antenna.

underlay approach). Although some antennas cover frequency band from $470 - 702\ MHz$ (the American standard), they will be listed as the aim of this section is to discover different techniques used to implement such antennas.

2.3.2.1 A Compact and Reconfigurable DVB-H Antenna for Mobile Handheld Devices

In [10], a DVB-H reconfigurable antenna was presented using a Printed Inverted F-Antenna (Printed-IFA). The antenna structure is shown in Fig. 2.12. The operating frequency could be adjusted to operate from $470 - 862\ MHz$ as shown in Fig. 2.13. The tunability was achieved using a varactor with capacitance range of $0.2 - 2\ pF$. A tunable voltage ranges from $0 - 22\ V$ was used to tune the varactor. A DC block capacitor was used to isolate the radiating element from the ground. The antenna had an omnidirectional radiation pattern with a planar structure of size $90 \times 35\ mm^2$.

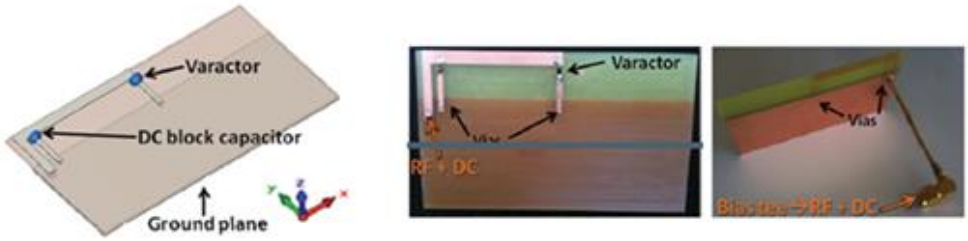

(a) **(b)**

Figure 2.12: (a) Structure of the antenna. (b) Fabricated antenna.

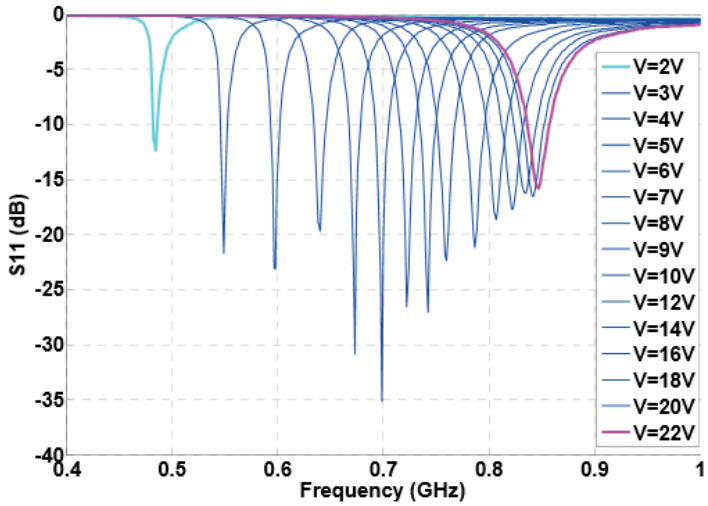

Figure 2.13: Measured $|S_{11}|$ for the antenna for different varactor values.

2.3.2.2 Reconfigurable Meander Antenna for DVB-H Band

In [11], a reconfigurable DVB-H antenna was proposed using a meander antenna. Tunability was achieved by using eight PIN diodes as show in Fig. 2.14. This antenna was designed to achieve eight bands to cover frequency from 470 –

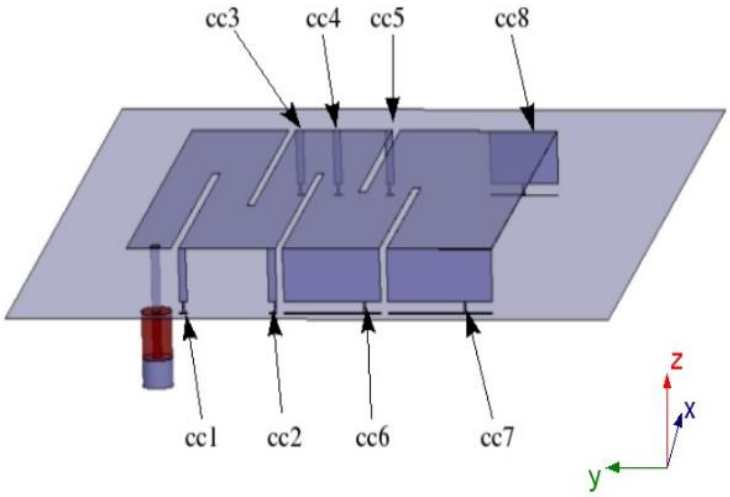

Figure 2.14: Structure of the antenna.

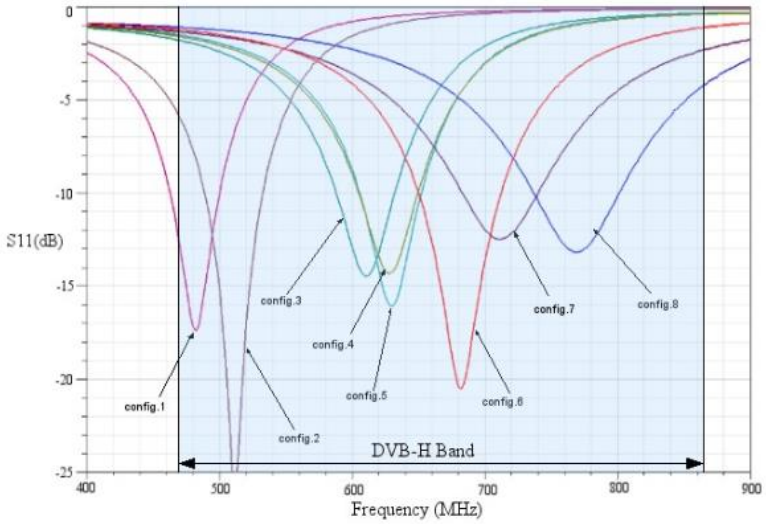

Figure 2.15: Measured $|S_{11}|$ for different switches configurations.

$702\ MHz$, as shown in Fig. 2.15. The antenna had an omnidirectional radiation pattern and a 3D structure of size $60 \times 49 \times 7\ mm^3$.

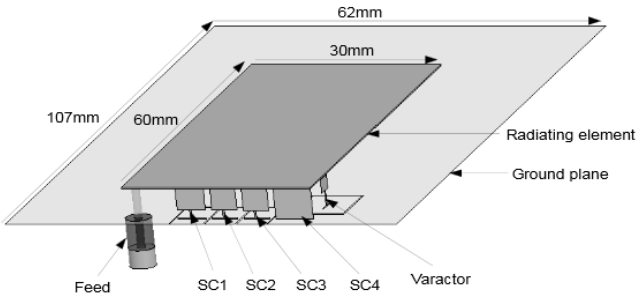

Figure 2.16: Structure of the antenna.

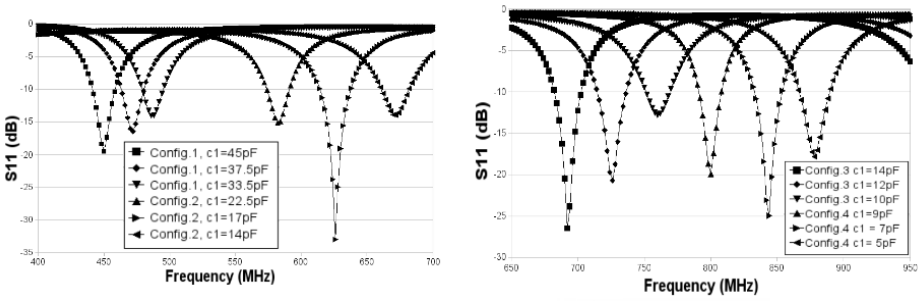

Figure 2.17: Measured $|S_{11}|$ for different switches configurations.

2.3.2.3 Reconfigurable Miniature Antenna for DVB-H Standard

In [12] a reconfigurable DVB-H antenna was proposed as shown in Fig. 2.16. In order to cover the spectrum from $470 - 862\ MHz$, both PIN diodes and varactor diodes were used. PIN diodes were used to divide the spectrum into four bands. The varactor diode was then used to tune the frequency in each band to meet the DVB-H specifications, as shown in Fig. 2.17. The varactor achieved a capacitance range of $5 - 40\ pF$ using a tuning voltage $0.4 - 20\ V$. The antenna had a size $107 \times 62\ mm^2$.

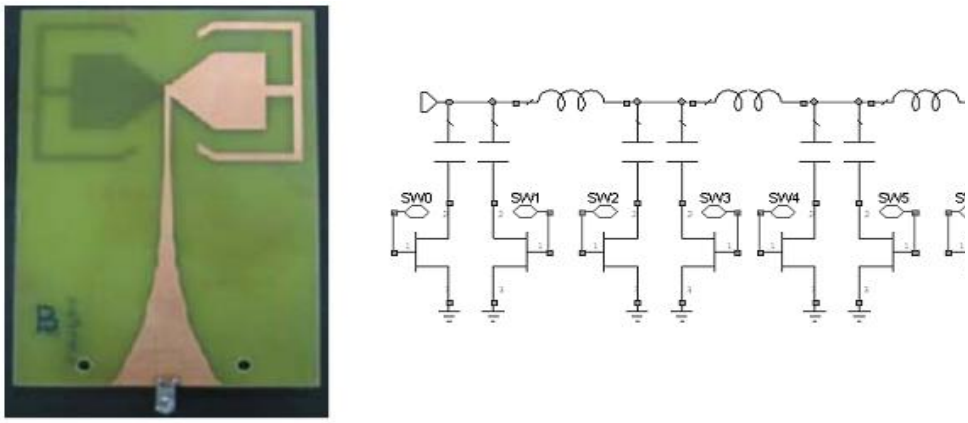

Figure 2.18: (a) Structure of the antenna. (b) The circuit used to match the antenna at different frequencies.

2.3.2.4 Application of an Impedance Tuning Network for Mobile DVB-H Terminals

In [13], a reconfigurable tuning antenna was proposed. The antenna was mainly a parallel-strip line with a balun feed. Tunability was achieved by using a tuning network to reduce the mismatch between the antenna and the RF-front-end (no change in the antenna, only in the circuit following it). Eight Micro-Electro-Mechanical Systems (MEMS) switches were used to cover the band from $470 - 702\ MHz$. These eight switches gave 256 possible states to cover all DVB-H channels. Fig. 2.18 (a) and (b) shows the structure of the antenna and the tuning network with the MEMS switches. Measured $|S_{11}|$ is shown in Fig. 2.19. The antenna had a planar structure of size $100 \times 60\ mm^2$.

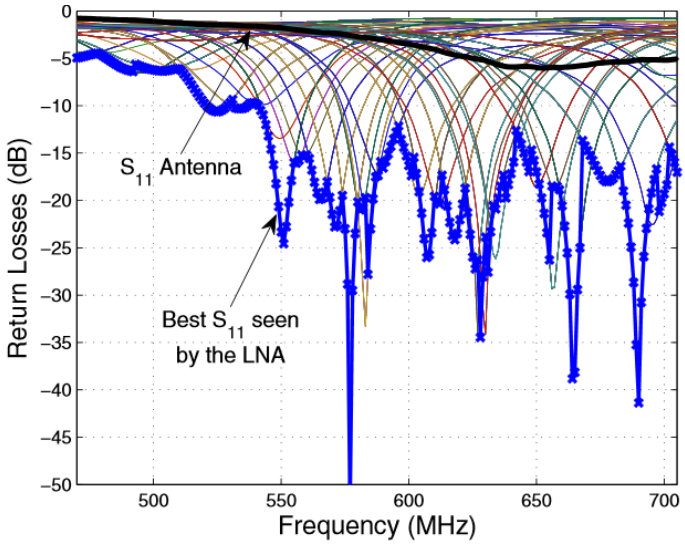

Figure 2.19: Measured $|S_{11}|$ for different switches configurations.

2.4 Spectrum Underlay CR

In the spectrum underlay CR, the secondary user is allowed to send signals with very low power over a large frequency band. Hence, he can simultaneously use the spectrum with the primary user. Only an UWB antenna is needed in this system. The main challenge is to minimize the antenna size, so it can be installed in portable devices. A survey for the techniques used to implement UWB antennas is carried. These antennas can be used in the spectrum underlay CR as well as in the spectrum interweave CR (as a sensing antenna).

2.4.1 UWB Antennas

The first UWB antenna was the biconical antenna presented by Oliver Lodge in 1898 [14]. This antenna was a bulky three dimensional structure. In 1950*'s*, frequency independent antenna was proposed by Rumsey [15]. In 1990*'s*, UWB antennas were proposed. Examples of this family are listed below.

2.4.1.1 Leaf-Shaped Monopole Antenna with Extremely Wide Bandwidth

In [16], a planar inverted cone antenna (PICA) was proposed, as shown in Fig. 2.20 (a). This antenna covered the frequency band from $1.3 - 29.7$ GHz with a planar structure size of $80 \times 80\ mm^2$. Fig. 2.20 (b) shows the measured $|S_{11}|$ for the antenna with and without the holes. These holes changed the current distribution on the monopole surface and resulted in wider impedance bandwidth.

2.4.1.2 Elliptical Planar Monopole Antenna with Extremely Wide Bandwidth

In [17], an elliptic shape monopole antenna with a trapizoform ground was proposed. This antenna was fed using coplanar waveguide (CPW) as shown Fig. 2.21 (a). It covered the frequency band from $0.41 - 8.86\ GHz$ as shown in Fig. 2.21 (b) with planar structure size of $139 \times 117\ mm^2$.

2.4.1.3 Printed Annular Monopole Antenna for Ultra-Wideband Applications

In [18] a monopole patch of an annular shape with a trapizoform ground was proposed. This antenna was fed using CPW as shown in Fig. 2.22 (a). It covered the frequency band from $0.6 - 10\ GHz$ as shown in Fig. 2.22 (b) with a planar structure size of $140 \times 140\ mm^2$.

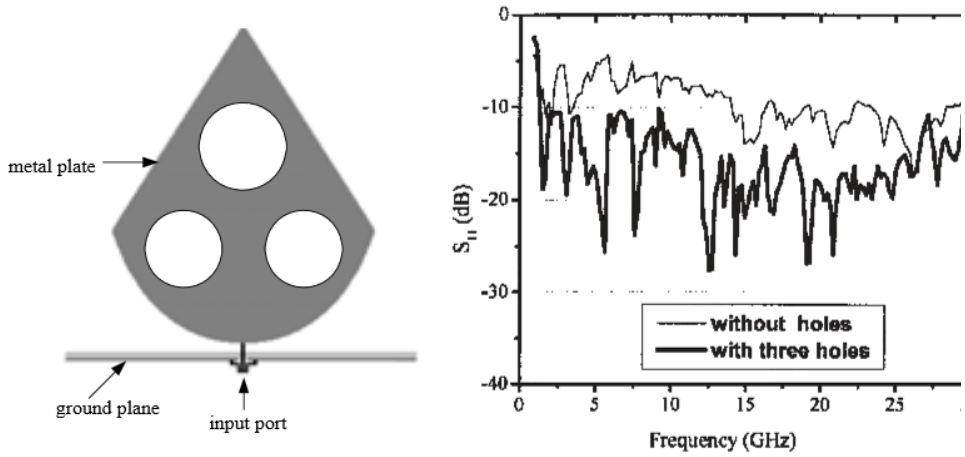

(a) **(b)**

Figure 2.20: (a) PICA structure. (b) Measured $|S_{11}|$ for the case of with and without holes.

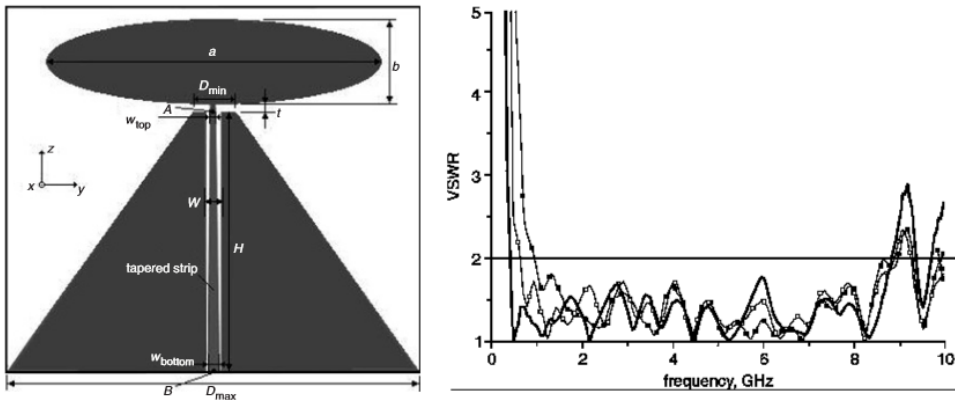

(a) **(b)**

Figure 2.21: (a) Structure of the antenna. (b) Simulated and measured VSWR.

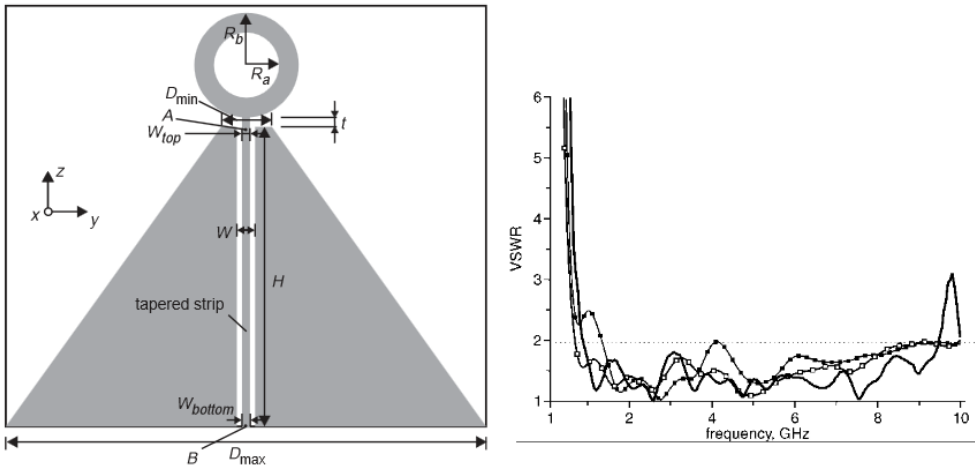

(a) **(b)**

Figure 2.22: (a) Structure of the antenna. (b) Simulated and measured VSWR.

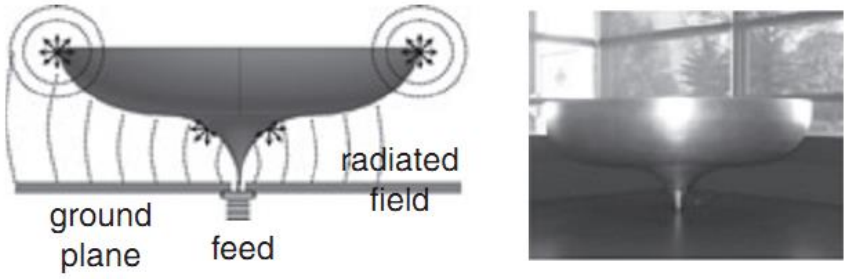

(a) **(b)**

Figure 2.23: Structure of the antenna. (b) Fabricated antenna.

2.4.1.4 Low-Profile Ultra-Wideband Inverted-Hat Monopole Antenna for 50 MHz–2 GHz Operation

In [19], an Inverted Hat Antenna was proposed. It covered the spectrum from $50\ MHz - 2\ GHz$ with a 3D structure size of $381 \times 381 \times 152\ mm^3$ as shown in Fig. 2.23.

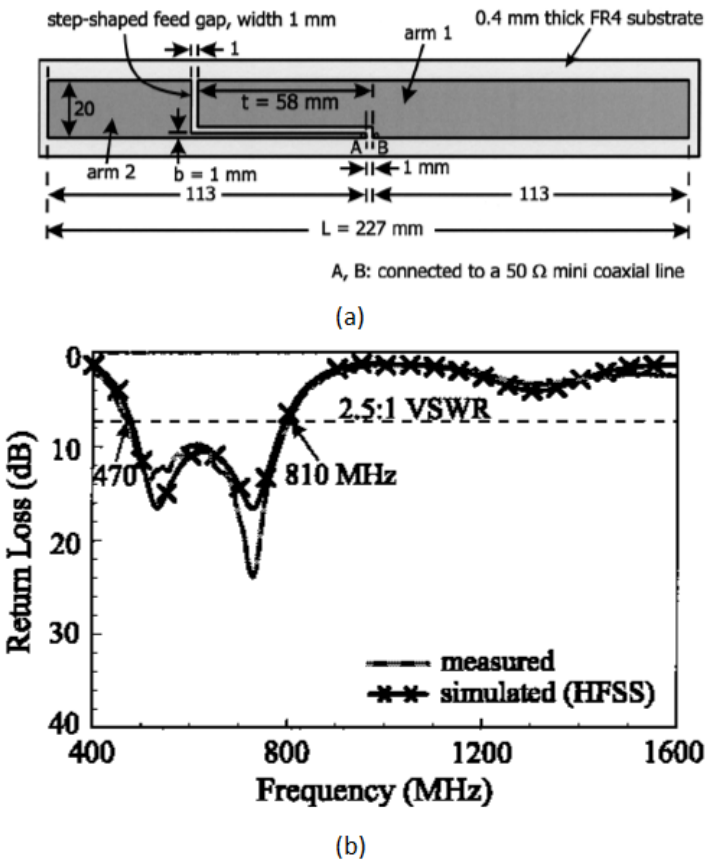

Figure 2.24: (a) Structure of the antenna. (b) Simulated and measured $|S_{11}|$.

2.4.1.5 Broadband Printed Dipole Antenna with a Step-Shaped Feed Gap for DTV Signal Reception

In [20], a step-shaped feed gap was used to implement a broadband planar dipole antenna covering frequency range from $470 - 806\ MHz$. The fact that there are two feeding points means that the wave entering at each point sees different dipole. Hence, two resonance frequencies were achieved ($530\ MHz, 730\ MHz$). The coupling between these two bands gave the wideband operation. The structure of the antenna and the simulated and measured $|S_{11}|$ are shown in Fig. 2.24 (a) and (b), respectively. The antenna had an omnidirectional radiation pattern with a planar structure of size $227 \times 20\ mm^2$.

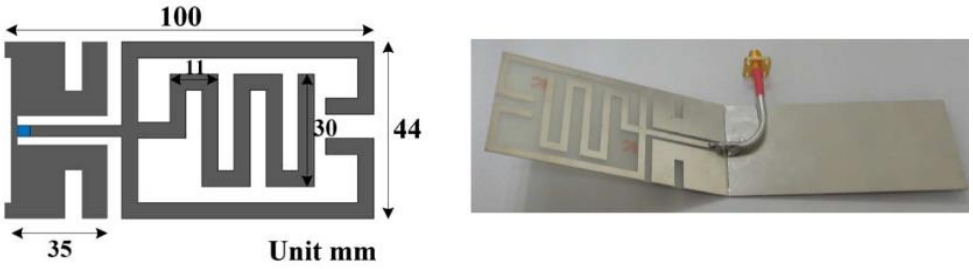

(a) **(b)**

Figure 2.25: (a) Structure of the antenna. (b) Fabricated antennas.

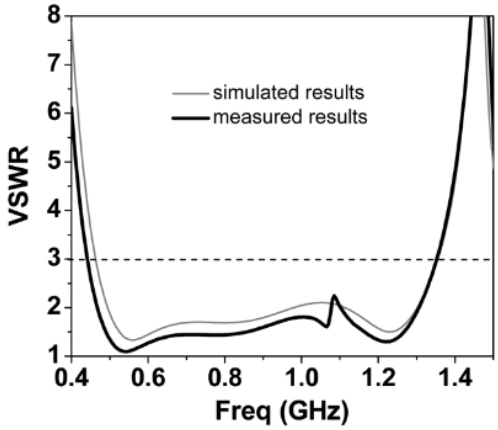

Figure 2.26: Simulated and measured VSWR.

2.4.1.6 Planar Meander Monopole Antenna with Parasitic Strips and Sleeve Feed for DVB-H/LTE/GSM850/900 Operation in the Mobile Phone

In [21], an UWB antenna covering the frequency range from $440 - 1350\ MHz$. was proposed. It was mainly a meander monopole with two parasitic strips. The width and the position of these strips were important factors to maximize the impedance bandwidth. The structure of the proposed antenna and the fabricated prototype are shown in Fig. 2.25 (a) and (b), respectively. The antenna had a planar structure of size $100 \times 44\ mm^2$. This antenna was designed to be installed in folded devices. Fig. 2.26 shows simulated and measured VSWR.

2.5 Results and discussion

Many techniques have been used to achieve reconfigurability and wideband operation. Table 2.1 summarizes these techniques.

Table 2.1: Summary of different techniques to achieve tunability and wideband operation.

Reconfigurability	
Concept	Method
Using differing antennas	Mechanical system (stepper motor) • Large size. • Limited speed. • Inefficient in practical designs.
Modifying antenna physical length (using switches)	PIN diodes • Controlled by DC line → affects the radiation characteristics of the antenna. • Limited number of channels.
	MEMS switches • Controlled by DC line → affects the radiation characteristics of the antenna. • Limited number of channels. • Needs access to MEMS technology.
	Optical switches • Controlled by a laser diode → radiation characteristics are not affected. • Limited number of channels

	• Adds some complexity to the design.
Modifying antenna electrical length	Variable capacitor (varactor diode) • Can be tuned to contentiously cover all channels in the band. • Large capacitance range is needed to cover the DVB-H band → requires high voltage range (up to 20 V). • High sensitivity to biasing voltage. • DC line is used to tune the varactor → affects the radiation characteristics of the antenna.

Wideband Operation	
Concept	Method
Coupling between two bands or more	Step-shaped feed gap
Optimizing the shape of the antenna.	Egg-shaped monopole antenna. Leaf-shaped monopole antenna. Inverted hat antenna.
All these antennas have large size (proportional to $\lambda/2$ of the lowest frequency).	

2.6 Conclusion

CR is an important technique to overcome the shortage in the RF spectrum caused by the static frequency allocation. Many systems have been implemented in the frequency band $1-10\,GHz$. Different techniques were used to achieve

reconfigurability and wideband operation. In the DVB-H band, no work was found to implement both reconfigurable and UWB antennas on the same substrate. On the other hand, many research groups have designed either reconfigurable or UWB antennas in the DVB-H band.

In this thesis, we target the spectrum underlay CR approach. Thus, we will design only an UWB antenna. This antenna should cover the entire DVB-H band with minimum size, high efficiency and omnidirectional pattern.

Since DVB-H operates in frequency band $0.47 - 0.86\,GHz$, it has a fundamental challenge concerning the size of the antenna. This challenge arises from the fact that the wavelength $(35 \sim 64\ cm)$ of this band is comparable to the dimensions of the portable devices. Thus, the use of miniaturization techniques is a must for these antennas.

As concluded form Table 2.1, the techniques used to implement UWB antennas did not reduce the size significantly (antenna size is proportional to wavelength of the lowest frequency). The concept of materials will be used to design a novel DVB-H compact size antenna (in chapter 5). This concept will be discussed in the next chapters.

Chapter 3
Metamaterial and Its Applications on Resonant Type Antennas

In this chapter, a brief introduction for metamaterial will be provided. First, metamaterial definition and historical milestones will be stated. Second, the unique properties that had led to this new class of material will be explained. Then, the work that inspired us will be mentioned. Lastly, the design of a novel multi-band antenna will be discussed.

Although wideband operation could not be achieved using techniques described in this chapter, the results were interesting enough to be accepted for publication in IEEE Antennas and Wireless Propagation Letters.

3.1 Introduction

"In a sense, every material is a composite, even if the individual ingredients consist of atoms and molecules. The original objective in defining a permittivity ε and permeability μ was to represent a homogeneous view of the electromagnetic

properties of a medium. Therefore, it is only a small step to replace the atoms of the original concept with structure on a larger scale." [22] This replacement is done under certain constrains leading to materials with different properties. In the following, an introduction for electromagnetic metamaterials based on the previous statement will be discussed.

3.1.1 Metamaterial Definition

Electromagnetic metamaterials are defined as "artificial effectively homogeneous electromagnetic structures with unusual properties not readily available in nature" [23]. These structures are periodic with building blocks called unit cells. The effectively homogeneous property means that the size of the unit cell is much less than the wavelength λ (usually $\lambda/4$ is taken as a reference), thus the electromagnetic wave senses only the macroscopic constitutive parameters which are defined by the unit cell itself. In other words, the electromagnetic wave is 'myopic' to detect the internal structure. Constitutive parameters (electric permittivity ε and magnetic permeability μ) are related to refractive index n by

$$n = \pm\sqrt{\varepsilon_r \mu_r}$$

where ε_r and μ_r are the relative permittivity and permeability, respectively. The $\pm$ sign indicates that there are four cases. Three of them represent the conventional materials (double positive and single negative). The double negative case (negative refractive index) means that the phase and group velocities are antiparallel (will be shown in next subsections). This means that the electric field $\bar{E}$, the magnetic field $\bar{H}$ and the phase constant $\bar{\beta}$ vectors build a left-handed (LH) triad (in the conventional materials, these vectors build a right-handed (RH) triad). Fig. 3.1 shows the four different cases for different sign combinations. The right and left-handed triads with the Poynting vector $\bar{S}$ (energy propagation

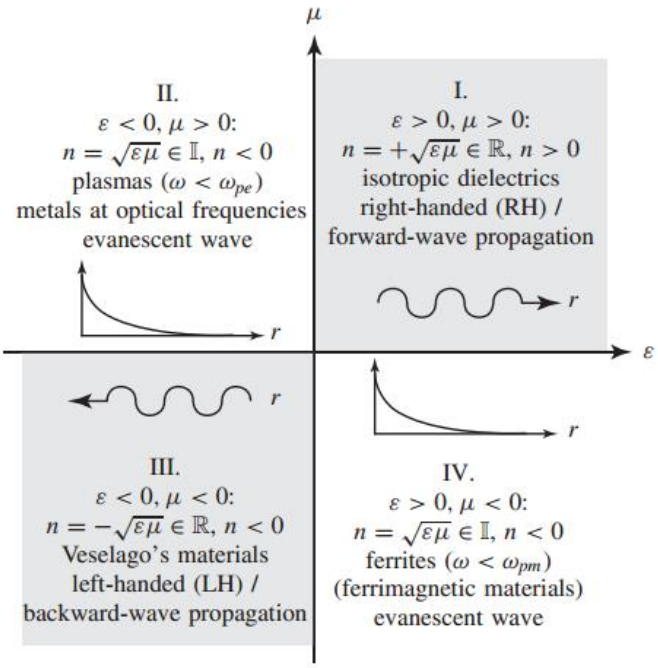

Figure 3.1: Permittivity-permeability (ε - μ) and refractive index (n) diagram. The four cases for different sign combinations are shown [23].

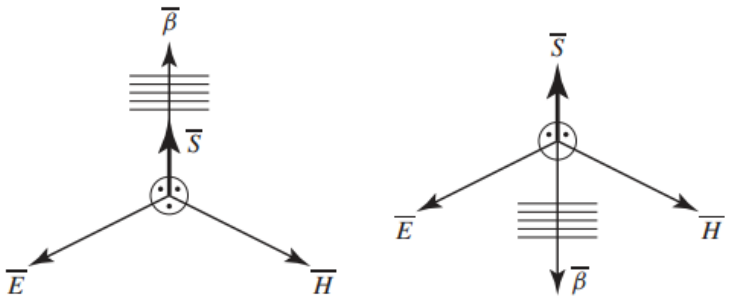

(a) **(b)**

Figure 3.2: Electric field-magnetic field-wave vector triad $(\bar{E}, \bar{H}, \bar{\beta})$, and Poynting vectors $\bar{S}$ for (a) RH, and (b) LH materials [23].

direction) are shown in Fig. 3.2. Thus, a new class of materials is defined as left-handed materials (LHM).

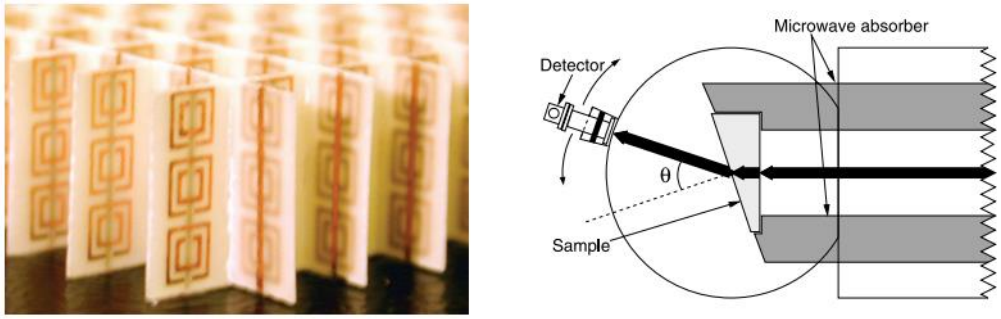

(a) **(b)**

Figure 3.3: Experimental verification of negative refractive index. (a) Photograph of the used LHM sample. (b) Diagram of the experiment setup. The black arrows represent the microwave beam as would be refracted by a positive index [24].

3.1.2 Brief Historical Review

In 1967, a Russian physicist Viktor Veselago discussed the potential of having a natural material that could have the LH triad property [24]. Thirty years later, a LHM was introduced for the first time by Smith and Colleagues at University of California, San Diego (UCSD). This material was artificial effectively homogeneous structure. In 2001, an experimental verification of a negative refractive index was done [25]. A LHM consisting of a two-dimensional array of unit cells, shown in Fig. 3.3 (a), was used. The unit cell consisted of a wire element (to produce negative ε [26]) and a split ring resonator (to produce negative μ [22]). A microwave beam (in X-band) was transmitted through a prism fabricated from this LHM. Using the structure in Fig. 3.3 (b), refraction angle was measured. Refractive index was determined according to Snell's law and found to be negative.

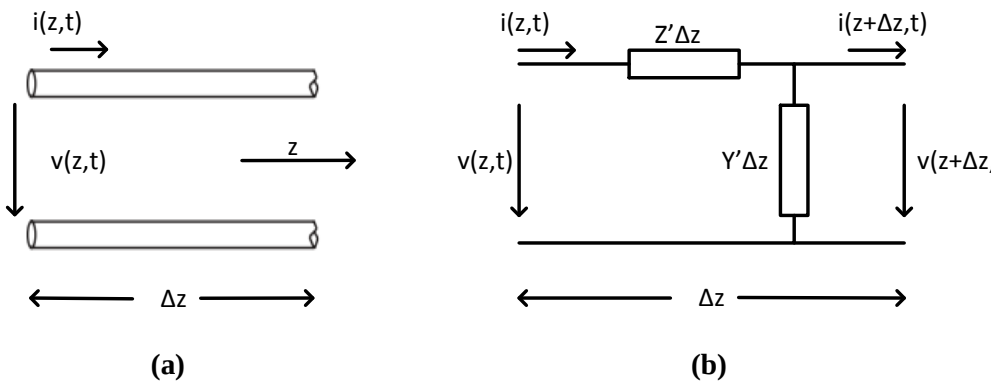

Figure 3.4: Incremental length of TL: (a) Voltage and current definition, and (b) lumped-element equivalent circuit.

3.2 Transmission Line Metamaterial Theory

The theory of transmission line (TL) metamaterials was first introduced in [23]. They are implemented by periodical repetition of a unit cell. To satisfy the homogeneity condition, the size of this unit cell Δz has to be much smaller than the guided wave length λ_g $\left(\Delta z \ll \lambda_g\right)$. The model of these TL metamaterials is a generalized form of the conventional TL model [27]. Fig. 3.4 shows a generalized model of TL. Z' and Y' are the per-unit length impedance and admittance. As in the well-established TL model, by applying both Kirchhoff's voltage and current law and taking the limit as $\Delta z \to 0$ for the circuit in Fig. 3.4 (b), Telegraphist's equations[4] are:

$$\frac{dV}{dz} = -Z'I \qquad (3.1a)$$

$$\frac{dI}{dz} = -Y'V \qquad (3.1b)$$

[4] These equations are driven for steady-state sinusoidal waves based on cosine phasors.

Where V and I are the position-dependent voltage and current along the line. By solving $(3.1a)$ and $(3.1b)$ simultaneously, V and I wave equations are found to be:

$$\frac{d^2V}{dz^2} - \gamma^2 = 0 \tag{3.2a}$$

$$\frac{d^2I}{dz^2} - \gamma^2 = 0 \tag{3.2b}$$

where $$\gamma = \alpha + j\beta = \sqrt{Z'Y'} \tag{3.3}$$

is the complex propagation constant. Traveling wave solutions to (3.2) are

$$V(z) = V_o^+ e^{-\gamma z} + V_o^- e^{+\gamma z} \tag{3.4a}$$

$$I(z) = I_o^+ e^{-\gamma z} + I_o^- e^{+\gamma z} = \frac{1}{Z_c}(V_o^+ e^{-\gamma z} - V_o^- e^{+\gamma z}) \tag{3.4b}$$

where

$$Z_c = \frac{Z'}{\gamma} = \sqrt{\frac{Z'}{Y'}} \tag{3.5}$$

is the characteristic impedance relating the voltage and current on the line as

$$Z_c = V_o^+ / I_0^+ = -V_0^- / I_0^-$$

According to Z' and Y', different types of TL can be realized as will be shown in the next subsections.

3.2.1 Purely Right-Handed (PRH) TL

This is a conventional lossless TL [27] and corresponds to the case of the ordinary material. It consists of a series inductance and parallel capacitance. Thus, $Z' = j\omega {L_R}'$ and $Y' = j\omega {C_R}'$, where ${L_R}'$ and ${C_R}'$ are the per-unit length inductance

and capacitance. The equivalent circuit model is shown in Fig. 3.5 (a). Substituting in (3.3) and (3.5) yields:

$$\beta_{PRH} = \omega\sqrt{L'_R C'_R} = \frac{\omega}{\omega'_R} \tag{3.6}$$

$$Z_{c_{PRH}} = \sqrt{\frac{L'_R}{C'_R}} \tag{3.7}$$

The dispersion relation found from (3.6) is plotted in Fig. 3.5 (b).

3.2.2 Purely Left-Handed (PLH) TL

The equivalent circuit model of this TL consists of a series capacitance and a parallel inductance, as shown in Fig. 3.6 (a) [23]. Thus, $Z' = 1/(j\omega C_L{}')$ and $Y' = 1/(j\omega L_L{}')$. Substituting in (3.3) and (3.5) yields:

$$\beta_{PLH} = -\frac{1}{\omega\sqrt{L'_L C'_L}} = -\frac{\omega'_L}{\omega} \tag{3.8}$$

$$Z_{c_{PLH}} = \sqrt{\frac{L'_L}{C'_L}} \tag{3.9}$$

Fig. 3.6 (b) shows the dispersion relation for the case of LHM found by (3.8). This ideal LH material cannot be realized in practice due to the existence of unavoidable RH parasitic effects. It should be noted that PLH TL has a negative phase velocity $\left(v_{ph} = \omega/\beta\right)$ and positive group velocity $\left(\frac{\partial\beta}{\partial\omega}\right)^{-1}$ as shown in Fig. 3.7.

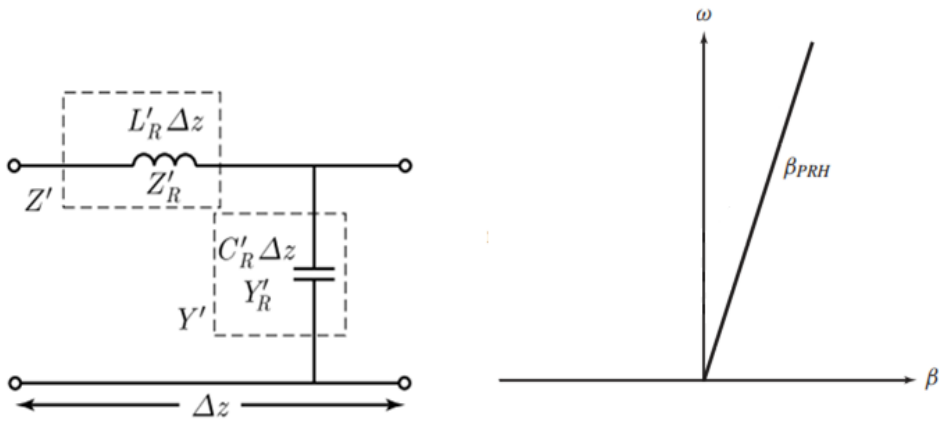

(a) **(b)**

Figure 3.5: (a) PRH TL equivalent circuit model. (b) Dispersion relation.

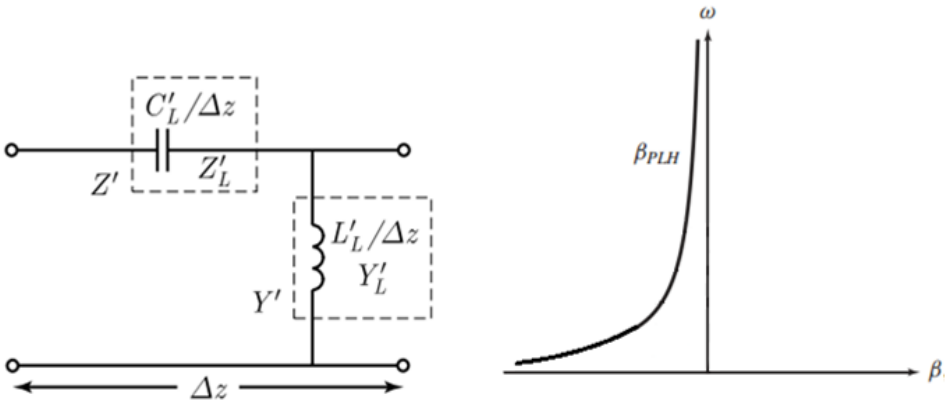

(a) **(b)**

Figure 3.6: (a) PLH TL equivalent circuit model. (b) Dispersion relation.

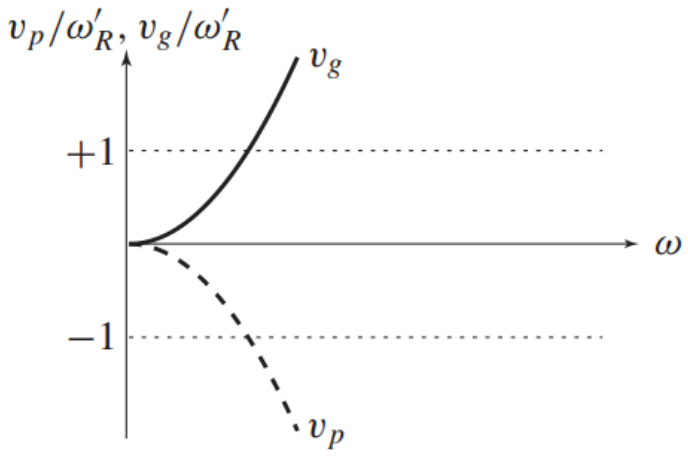

Figure 3.7: Phase and group velocities for PLH TL.

3.2.3 Conventional Composite Right/Left-Handed (C-CRLH) TL

The CRLH TL equivalent circuit model is shown in Fig. 3.8 (a) [23]. It is a combination of both RH and LH TL's. Z' and Y' are given by the following relations:

$$Z' = j\left(\omega L'_R - \frac{1}{\omega C'_L}\right) \tag{3.10}$$

$$Y' = j\left(\omega\, C'_R - \frac{1}{\omega L'_L}\right) \tag{3.11}$$

By substituting in (3.3) γ is found to be

$$\gamma = \alpha + j\beta = js(\omega)\sqrt{\left(\frac{\omega}{\omega'_R}\right)^2 + \left(\frac{\omega'_L}{\omega}\right)^2 - \kappa{\omega'_L}^2} \tag{3.12}$$

where $\kappa = L'_R C'_L + L'_L C'_R$

$$s(\omega) = \begin{cases} -1 & if \quad \omega < \min(\omega_{se}, \omega_{sh}) \quad LH\ range \\ +1 & if \quad \omega > \max(\omega_{se}, \omega_{sh}) \quad RH\ range \end{cases}$$

ω_{se} and ω_{sh} are the series and shunt resonance frequencies and given by the following relations:

$$\omega_{se} = \frac{1}{\sqrt{L'_R C'_L}}$$

$$\omega_{sh} = \frac{1}{\sqrt{L'_L C'_R}}$$

Although the TL is loss-less, (3.12) shows that γ can be purely real (stop band) as well as the purely imaginary case (pass band). The CRLH dispersion relation curve is shown in Fig. 3.8 (b). The following notes can be depicted:

1- At high frequency, this curve tends to the PRH dispersion, while at low frequency, it tends to the PLH dispersion.

2- For $\omega < \min(\omega_{se}, \omega_{sh})$, the phase velocity and the group velocity have opposite signs (antiparallel). For $\omega > \max(\omega_{se}, \omega_{sh})$, they have the same sign (parallel), as shown in Fig. 3.9 (a).

3- The frequency at which maximum attenuation occurs is $\omega_o = \sqrt{\omega'_R \omega'_L}$.

4- By substituting in (3.5), Z_c is found to be

$$Z_c = Z_{c_{PLH}} \sqrt{\frac{(\omega/\omega_{se})^2 - 1}{(\omega/\omega_{sh})^2 - 1}} \qquad (3.13)$$

Equation (3.13) is plotted versus w in Fig. 3.9 (b). It can be seen that Z_c is purely imaginary in the stop band while in the pass band, it is purely real.

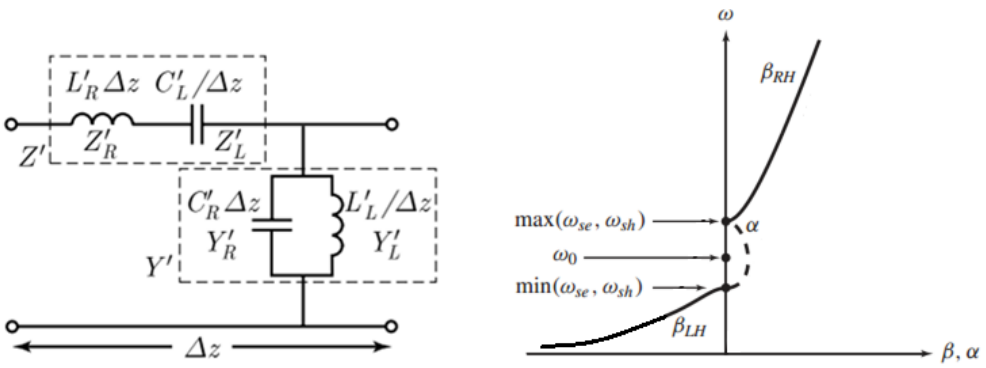

(a) **(b)**

Figure 3.8: (a) CRLH TL equivalent circuit model. (b) Dispersion relation.

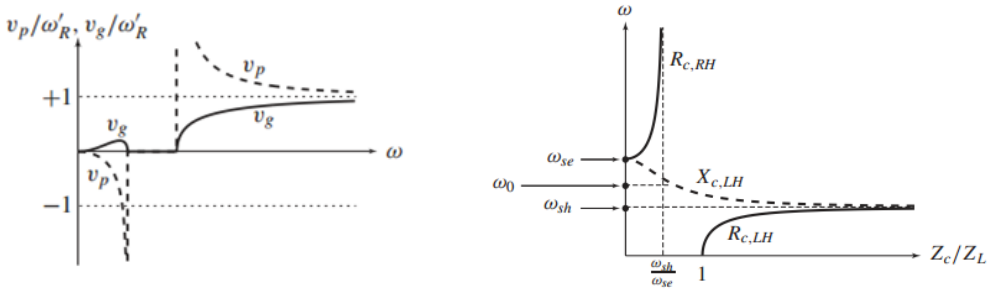

(a) **(b)**

Figure 3.9: CRLH TL: (a) Phase and group velocities. (b) Characteristic impedance.

3.2.4 Other TL Metamaterials

Fig. 3.10 shows other topologies for the TL equivalent circuit model. Dual CRLH (D-CRLH) [28] and Extended CRLH (E-CRLH) [29] are shown in Fig. 3.10 (a) and (b), respectively. The same procedure can be done to find these TL parameters. Although these TLs will not be used in this thesis, they are mentioned for the sake of completeness.

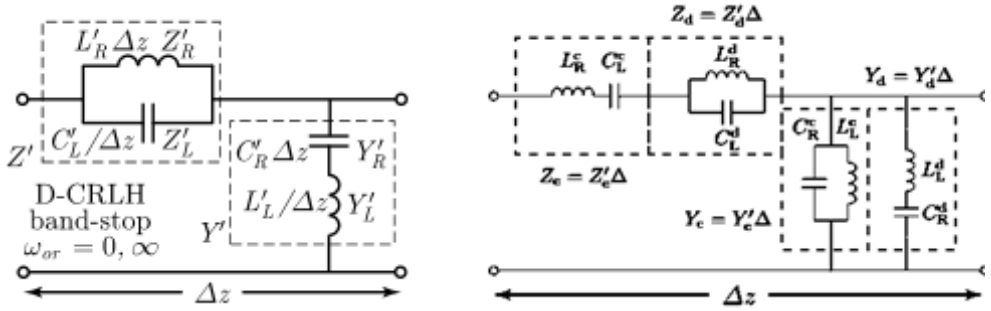

(a) **(b)**

Figure 3.10: Equivalent circuit model for (a) D-CRLH TL, and (b) E-CRLH TL.

3.3 Previous Work

In [30], [31], a new class of metamaterial-inspired antennas was proposed. It consists of a conventional microstrip-fed antenna loaded with CRLH-unit cells to achieve multiband operation, while maintaining a monopole-like radiation pattern at all bands. The main idea was to adjust the dispersion relation of the unit cell such that the total phase shift of the new antenna (the monopole and the unit cells) satisfies the following equation:

$$\varphi_{total} = \varphi_{monopole} + m \times \varphi_{CRLH} = n \times 90 \quad : n = 0, \pm 1, \pm 2, \ldots \qquad (3.14)$$

Where $\varphi_{monople}$, φ_{CRLH}, and m are the phase shift of the unloaded monopole, the phase shift of the CRLH unit cell, and the number of CRLH unit cells, respectively.

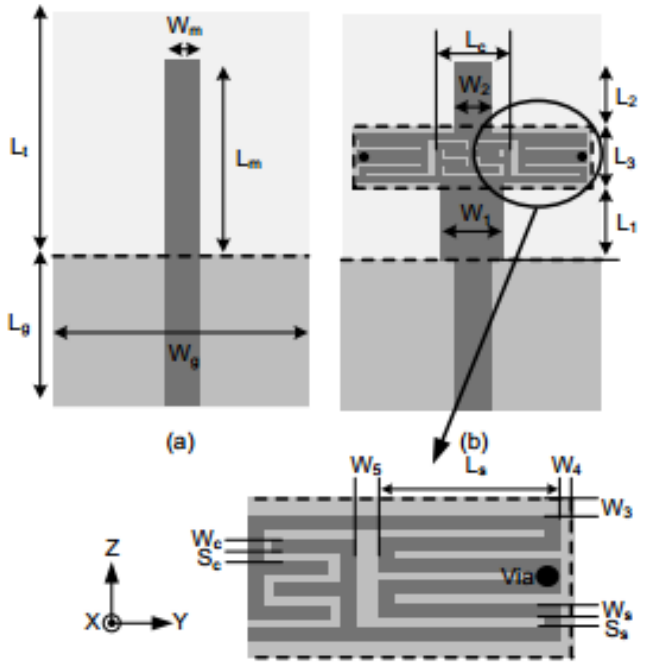

Figure 3.11: (a) Conventional microstrip-fed monopole antenna. (b) Microstrip-fed monopole antenna loaded with a CRLH unit cell.

Fig. 3.11 (a) and (b) shows the monopole antenna in both unloaded and loaded cases. The CRLH unit cell was realized using an interdigital capacitor to provide the series capacitance and a shunt short-circuited (through vias) stub to provide the parallel inductance. The series inductor and shunt capacitance are provided by the unavoidable parasitic RH behavior. The interdigital capacitor also contributed to the series inductor (as its equivalent circuit model is series LC). The unit cell was designed to have symmetry around the longitudinal axis of the monopole antenna. Thus, the monopole radiation pattern was not affected (the radiation of the right half cancels that of the left half, and hence, the radiation pattern is controlled mainly by the monopole).

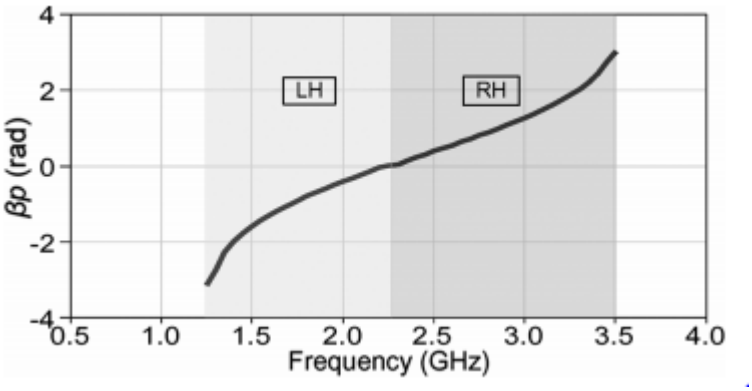

Figure 3.12: Dispersion relation of the CRLH unit cell.

The monopole was designed to radiate at 2.3 GHz. After adding the CRLH unit cell, four bands were achieved. These bands were explained based on the unit cell dispersion relation shown in Fig. 3.12 as follows: at low frequency corresponding to the lower stop band of the unit cell, the capacitor is almost open circuited. Thus the antenna behaved as an inductance loaded monopole. The second band was located within the LH region of the unit cell. In this region, the unit cell adds phase-advance which is exactly equal to the phase-lag provided by the monopole itself. Thus the total phase satisfies (3.14) with $n = 0$. The third band was the normal band of the monopole itself as the unit cell adds zero phase shift. This corresponds to $n = 1$ in (3.14). The last band was located within the upper edge of the RH region. This band is the monopole second resonance. The large phase-lag provided by the unit cell is the reason of lowering the resonance frequency. This corresponds to $n = 3$ in (3.14). These four bands as well as the unloaded case resonance frequency are shown in Fig. 3.13. It should be noted that it is not scientifically true to apply the concept of the dispersion relation (since there is only one unit cell), yet, it gives a good indication to start the design.

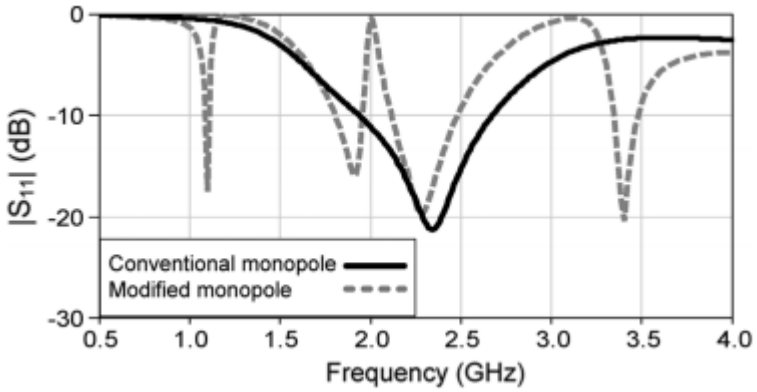

Figure 3.13: Simulated $|S_{11}|$ for both unloaded (solid line) and loaded (dashed-line) monopole antenna.

3.4 Resonant Type Antennas Loaded With CRLH Unit Cell

In this section, we show that using CRLH unit cells to enhance the antenna performance is not pertinent to monopole antennas only, but can be applied to other resonant type antennas as well. First, the concept is applied to the loop antenna and then applied to the printed-Inverted F Antenna (Printed-IFA).

In both cases, the CRLH unit cell is designed such that the loaded antennas occupy exactly the same size as the unloaded ones so that multi-band operation can be obtained with virtually no cost except for a minor deviation in the radiation patterns.

3.4.1 Loop Antenna Loaded with CRLH Unit Cell

The proposed loop antenna is shown in Fig. 3.14. It is basically a printed loop antenna fed by coplanar strip (CPS) transmission line and loaded with one half of the CRLH unit cell presented in [30]. As stated before, one of the main reasons that unit cell was made symmetric is to minimize its radiation, and hence, the

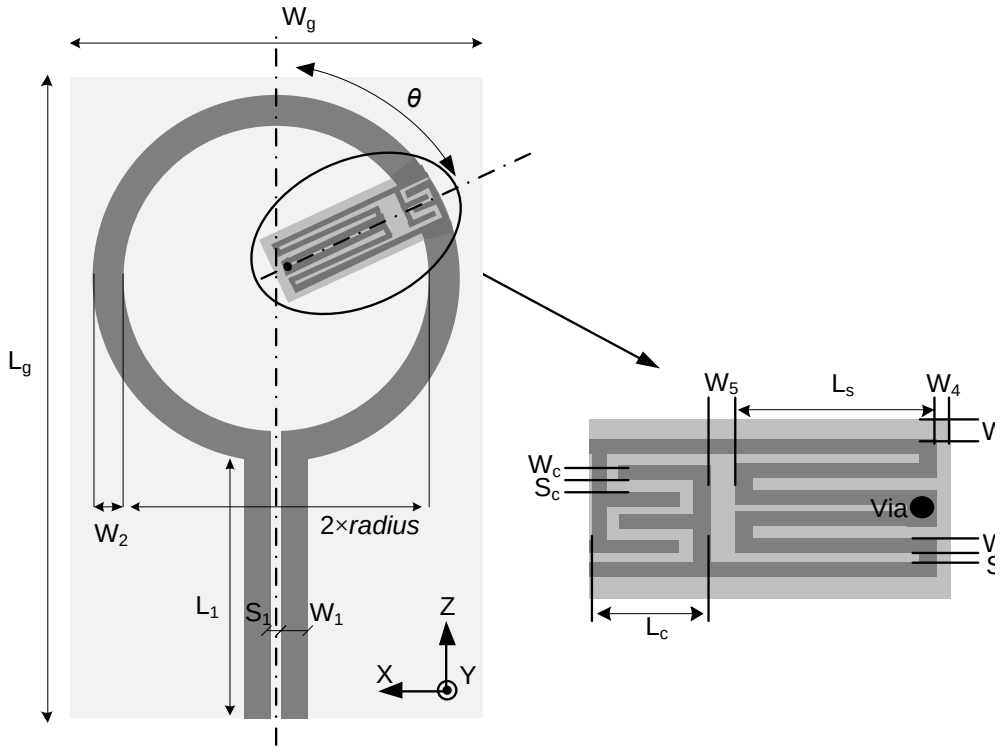

Figure 3.14: Proposed loop antennas loaded with CRLH unit cell.

radiation pattern is controlled mainly by the monopole. This came at the expense of large size in the lateral direction. In the case of loop antenna, only one half of the unit cell is used in order to best utilize the area inside the loop at the expense of altering the radiation pattern.

The design starts by loading the antenna with a lumped-component CRLH unit cell, shown in Fig. 3.8 (a). The components values are determined to achieve three resonance frequencies in the stop, left, and right -handed bands respectively. The dimensions of the interdigital capacitor and meandered inductors are then adjusted to achieve the same dispersion relation as that of the lumped-component counterpart. One should note that these dimensions have to be changed a little

after loading the antenna with the CRLH in the EM simulator to adjust the resonance frequencies.

The loop antenna is designed on Rogers 5870 with substrate thickness (h) of 1.57 mm and a relative dielectric constant (ε_r) of 2.33. All dimensions are given in Table 3.1. The antenna exhibits two narrow bands at 0.925 GHz and 1.57 GHz, in addition to a wideband ranging from $1.9 - 2.9\ GHz$. Thus, the antenna can cover GSM900, UMTS, Bluetooth, WiFi (2.4 GHz), WiMAX (2.5 GHz) and GPS (1.57 GHz) bands (the unloaded loop is designed to resonate at $2.4\ GHz$). Antenna simulations are carried out on HFSS $V.13$. Fig. 3.15 shows the simulated $|S_{11}|$ for both unloaded and loaded loop antenna. Simulated radiation patterns for the loaded loop antenna are shown in Fig. 3.16 at the three operating bands. They vary from one frequency to another.

As explained in [32], [33] one-wavelength loop antenna has an E_φ component as shown in Fig. 3.15 (2.4 GHz). The strong presence of E_θ indicates that the unit cell alters the current distribution along the circumference and also there is radiation due to the current flowing in it. This was not observed in the monopole loaded with CRLH unit cell presented in [30] since the monopole preserve its donut-shaped radiation patterns for all frequencies that satisfy $l_{monopole} < \lambda/4$, and the unit cell was symmetrical such that it did not contribute to radiation. Also, it can be noticed that the radiation patterns are nearly symmetric although the position of the unit cell is not on the loop axis of symmetry. This indicates that the position of the added unit cell has a minor effect on the radiation pattern.

Finally, it is possible to load the loop antenna with more than one CRLH unit cell similar to [31]. This is especially attractive for the loop antenna due to the large available space inside the loop, and hence, more radiating bands can be

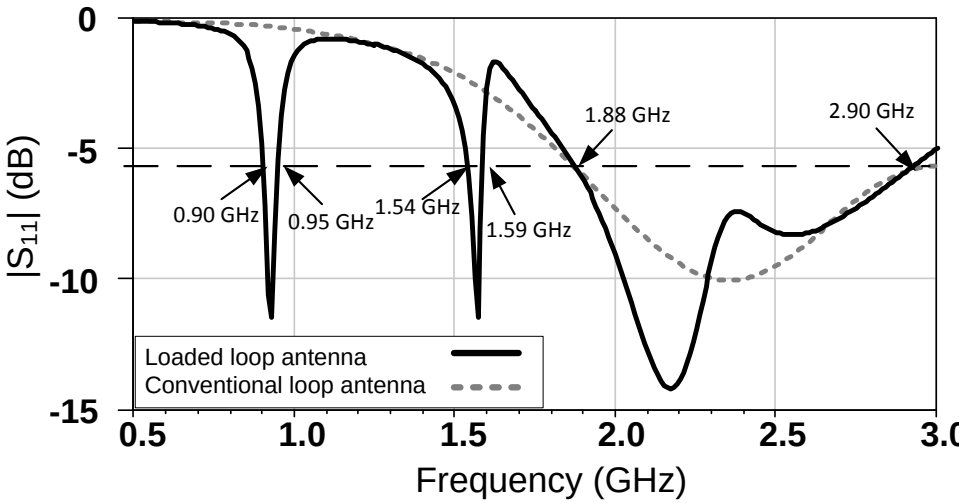

Figure 3.15: Simulated $|S_{11}|$ for loaded loop antenna (solid black line) and for unloaded loop antenna (dotted gray line).

obtained with no size penalty. This antenna was not fabricated to avoid the implementation of a very wideband balun working from $0.9 - 2.9\ GHz$.

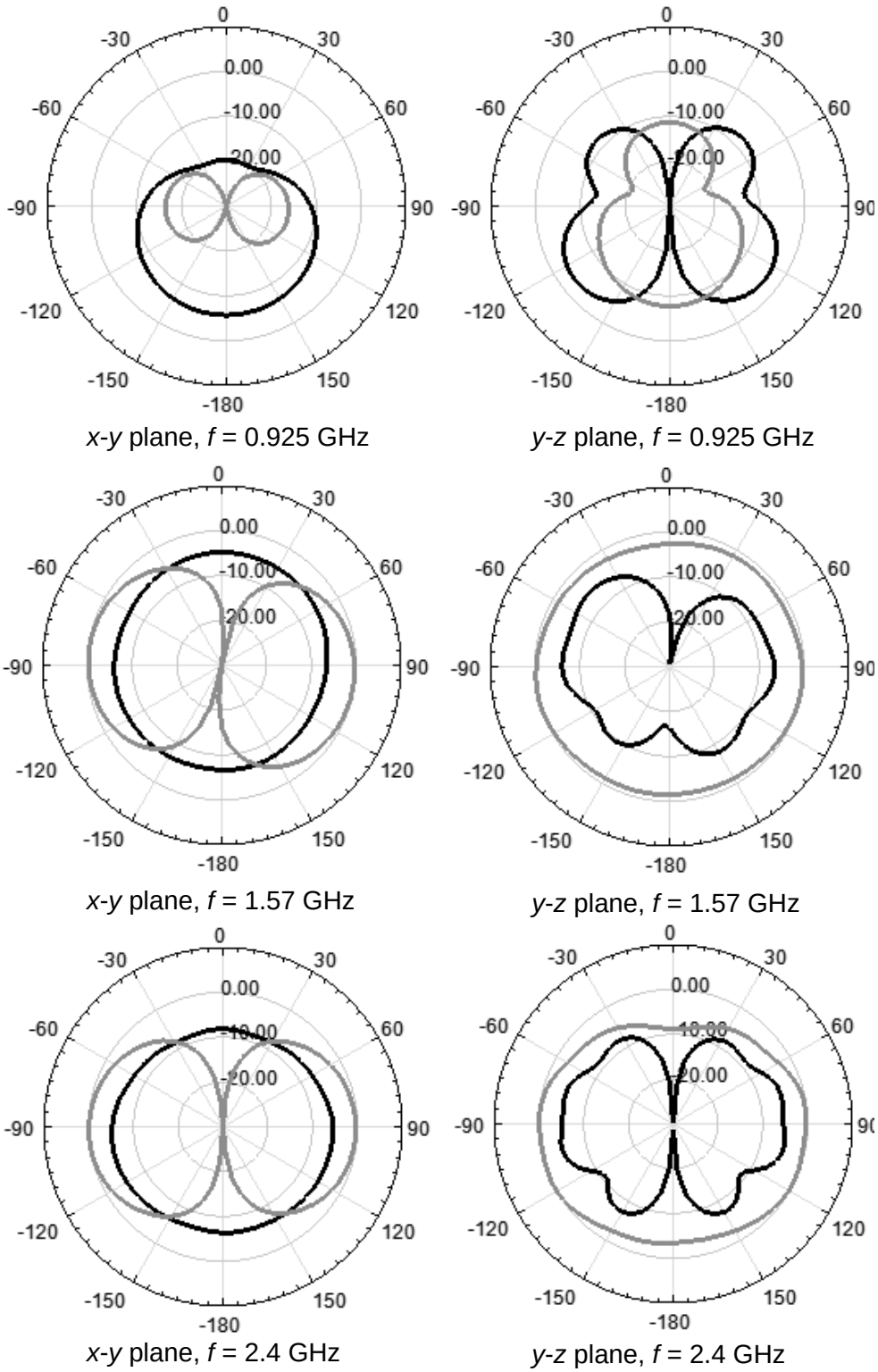

Figure 3.16: Simulated normalized radiation patterns, on dB scale, for the loop antenna at the three bands with black lines for E_θ and gray lines for E_φ. Axis is shown in Fig. 3.14.

3.4.2 Printed IFA Loaded with CRLH Unit Cell

Conventional printed IFA can be considered as a bent monopole to make the size more compact. As this bending introduces an extra capacitance between the radiator and the ground, a stub is used to cancel out this effect and maintain the resonance frequency [33]. The proposed printed IFA loaded with the CRLH unit cell is shown in Fig. 3.17. Again, only half of the CRLH unit cell is used for size reduction. Additionally, the unit cell is modified by implementing the shunt meandered inductance in the lower ground plane. Using this modified CRLH unit cell, the loaded printed IFA has exactly the same size as a conventional printed IFA operating at 1.7 GHz. The size of the conventional printed IFA ground plane is optimized based on the guide lines presented in [34] for printed monopole antennas.

The printed IFA antenna is designed on Rogers 5870 substrate to have a performance similar to the previous loop antenna. All dimensions are given in Table 3.1. The fabricated structure is shown in Fig. 3.18. S-parameter measurements are carried out on Rhode&Schwartz vector network analyzer ($ZVB-14$). The simulated and measured $|S_{11}|$ together with the simulated and measured far field radiation patterns are shown in Fig. 3.19 and Fig. 3.20, respectively. For the three bands, the reflection coefficient is better than $-10\ dB$. The third resonance is shifted from $1.7-1.95\ GHz$ because at $1.95\ GHz$ the CRLH unit cell provides zero phase shift and hence, the printed IFA's actual length is shorter than that of the unloaded printed IFA. Measured and simulated radiation patterns are in good agreement at the second and third bands. Some discrepancy appears at the first band that may be attributed to the inadequate size of the absorbers in addition to poor isolation. Fig. 3.21 shows the fabricated antenna in the anechoic chamber.

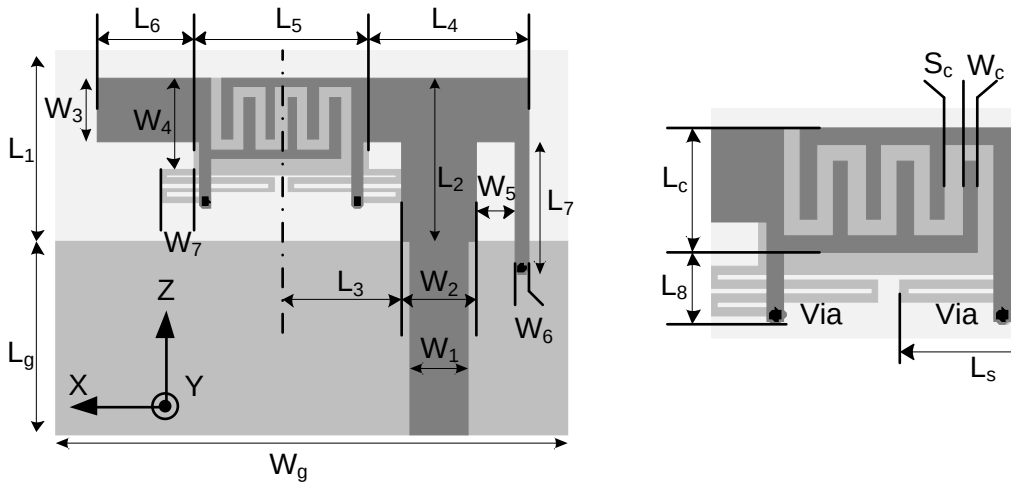

Figure 3.17: Proposed printed IFA antennas loaded with CRLH unit cell.

Efficiency is measured using different Wheeler-cap methods [35] - [38]. Table 3.2 shows the peak simulated and measured efficiencies within each band. Fluctuations between different Wheeler-cap methods are about 2%.

Compared to trap antennas presented in [39], [40], the proposed printed-IFA has an extra band (the second one) at which the phase of the unit cell compensates the phase of the host antenna [31].

(a) **(b)**

Figure 3.18: Picture of the fabricated printed IFA: (a) top side and, (b) bottom side.

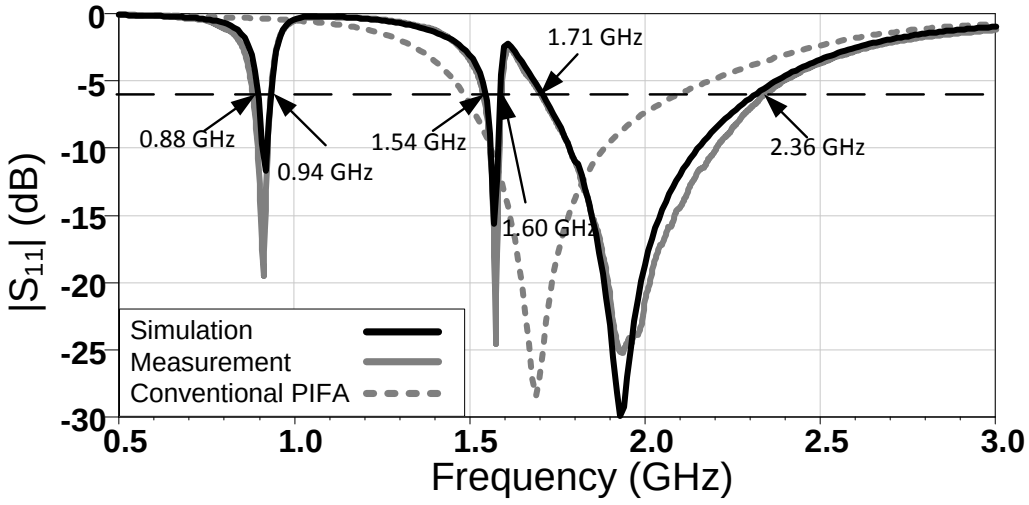

Figure 3.19: Simulated and measured $|S_{11}|$ for the loaded printed IFA (solid black and gray lines, respectively) and simulated $|S_{11}|$ for the unloaded printed IFA (dotted gray line).

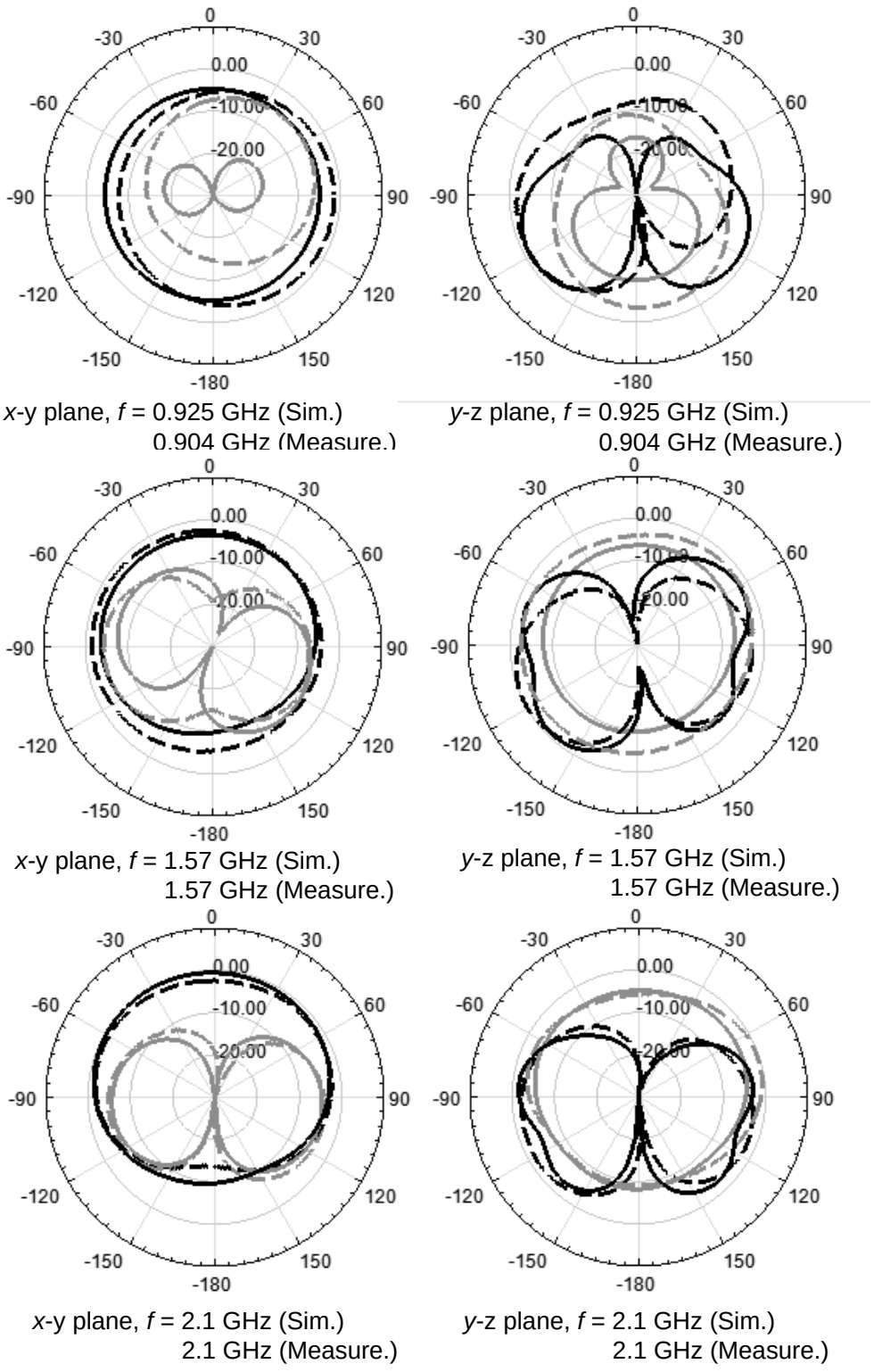

Figure 3.20: Simulated and measured normalized radiation patterns, on dB scale, for the printed IFA at the three bands with black lines as E_θ and gray lines for E_φ (simulation is plotted with solid lines and measurement is plotted with dashed lines). Axis is shown in Fig. 3.17.

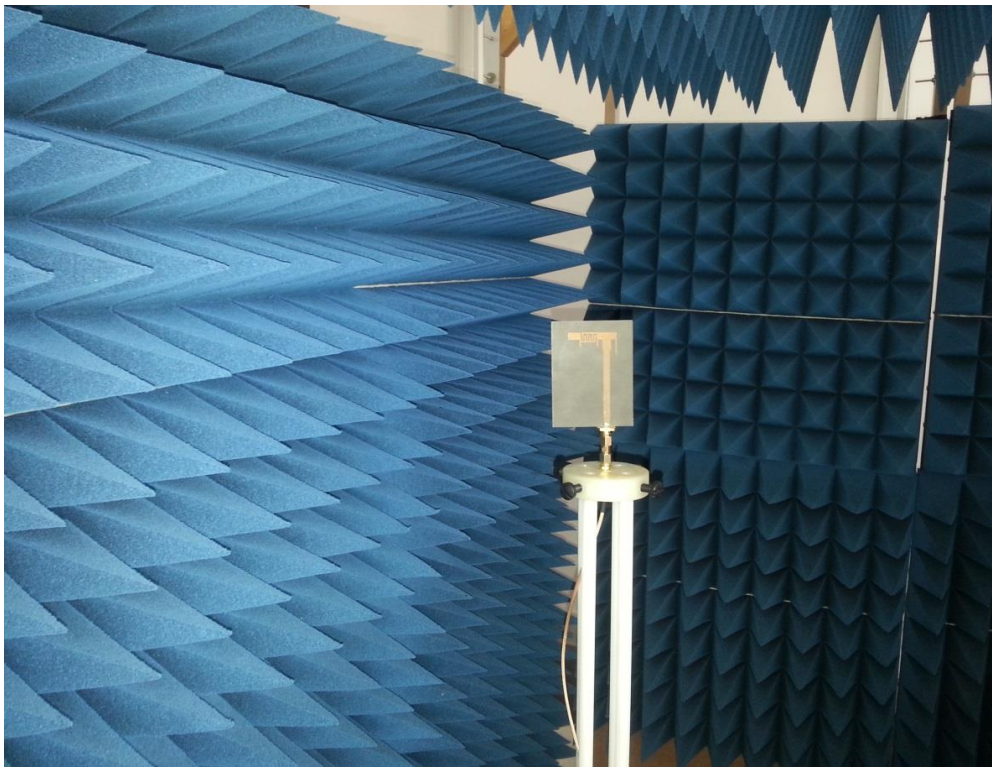

Figure 3.21: Picture of the fabricated printed IFA in the anechoic chamber.

Table 3.1: Dimensions of the loop and printed IFA antennas (in mm).

Symbol	Loop Antenna	Printed IFA
L_g	95	51
W_g	65	56
L_1	31	21
L_2	-	13
L_3	-	9.3
L_4	-	12.5
L_5	-	13.7
L_6	-	7.5
L_7	-	10.5
L_8	-	3.8
S_1	0.7	-
radius	19	-
Θ	75°	-
W_1	2	4.5
W_2	9	6
W_3	0.5	5
W_4	1	7.3
W_5	1.5	3
W_6	-	1
W_7	-	3.2
L_c	17.5	6.5
W_c	0.55	0.9
S_c	0.3	0.9
L_s	3.15	8.8

W_s	0.47	0.4
S_s	0.3	0.3
area (mm^2) (band I)	$\pi * (radius + W_2)^2 = \pi(0.084\lambda_1)^2$	$L_1 * (L_4 + L_5 + L_6) = 0.063\lambda_1 * 0.101\lambda_1$
area (mm^2) (band II)	$\pi(0.147\lambda_2)^2$	$0.110\lambda_2 * 0.176\lambda_2$
area (mm^2) (band III)	$\pi(0.187\lambda_3)^2$	$0.140\lambda_3 * 0.225\lambda_3$

*λ_1, λ_2 & λ_3 are the free space wave lengths calculated at 0.9, 1.57 and 2 GHz, respectively.

Table 3.2: Simulated and measured efficiency at two frequencies

Frequency (GHz)	BW	Simulated efficiency (%)	Measured efficiency (%)
0.91	0.88-0.94 GHz	81	80
1.56	1.54-1.60 GHz	83	80
2.04	1.71-2.36 GHz	99	94

3.5 Conclusion

The concept of loading resonant type antennas with CRLH unit cell was demonstrated. Specifically, two examples were considered, namely the loop

antenna and Printed IFA. For both cases, the antenna was tailored to have two narrow bands at 0.925 GHz and 1.57 GHz, and one wideband around 2.4 GHz. The CRLH unit cells were modified so that the loaded antenna occupies the same area as the unloaded one and, hence, more operating bands can be obtained with no size penalty. The unsymmetrical CRLH unit cells were verified not to have major effect on the radiation patterns of the antennas. A prototype printed IFA was fabricated to verify the concept. Simulations and measurements are in a good agreement.

Although wideband operation could not be achieved, the results were interesting enough to be accepted for publication IEEE Antennas and Wireless Propagation Letters.

Different approach to design antennas using metamaterials will be discussed in next chapters.

Chapter 4
Metamaterial Inspired Electrically Small Antennas

In the previous chapter, antennas were loaded with a CRLH unit cell to achieve multi-band operation. In this chapter, different approach, called metamaterial inspired electrically small antennas (ESA), is used to design compact size antenna. This approach will be extended in the next chapter to design compact size, DVB-H antenna.

This chapter serves as a survey on the progress in the metamaterial inspired antennas. It starts with some important definitions that will be used throughout the chapter. Then, different 2D and 3D realizations will be listed. Lastly, some important applications for these antennas will be mentioned.

4.1 Definitions

4.1.1 Metamaterial Based/Inspired Antennas

Metamaterial based means that the performance of a bare electric (magnetic) radiator is modified by surrounding it with ENG (MNG) or DNG[5] spherical shell. Metamaterial inspired means that this spherical shell is replaced with a metamaterial inspired unit cell placed in the very near field of this radiator. Many examples will be discussed in the following sections.

4.1.2 Electrically Small Antennas (ESAs)

Antenna enclosed within a sphere with effective radius r_e is considered electrically small if the following condition is satisfied:

$$kr_e \leq 1 \tag{4.1}$$

where k is the free space wave number. In other words, if it is contained within the Wheeler radian sphere[6]. If the antenna is designed with infinite ground plane, it will be electrically small if:

$$kr_e \leq 0.5 \tag{4.2}$$

4.1.3 Chu Limit

Chu limit defines a lower limit for the radiation quality factor, which in turns defines the upper limit for fractional BW (FBW) of the ESA enclosed in the Wheeler radian sphere. The minimum quality factor and maximum FBW are given by [41]

[5] ENG, MNG and DNG are abbreviations for Epsilon negative, Mu negative and double negative, respectively. Although metamaterial is defined for the case of double negative, many authors use it to describe single negative case as well [23].

[6] Wheeler radian sphere measures the boundary between the near and far fields of an ESA and its radius is given by $r_w = \lambda/2\pi$

$$Q_{che} = \frac{1}{(kr_e)^3} + \frac{1}{kr_e} \quad \& \quad FBW = \frac{1}{Q_{che}} = \frac{\Delta f_{3dB}}{f_{res}} \tag{4.3}$$

4.1.4 Equivalent Circuit of an Antenna

Any antenna can be considered as an RLC resonant circuit [32]. The resonance frequency is determined by

$$f_{res} = \frac{1}{2\pi\sqrt{C_{eff}L_{eff}}} \tag{4.4}$$

where C_{eff} and L_{eff} are the effective capacitance and inductance of the whole antenna system. All antennas in this chapter obey the previous definitions.

4.2 Proving the Concept

The electrically small electric dipole antenna is not an efficient radiator as it has a very small radiation resistance and a very large capacitive reactance [41]. To make it an efficient one, a very large inductance is needed to cancel out the capacitive part. After that, the whole system needs be matched to the $50\ \Omega$ source using any matching technique as shown in Fig. 4.1 (a). The problem is that the resulting system (the antenna and the matching network) is not electrically small anymore.

A new approach was proposed in [42]. An electrically small electric dipole antenna with length $\lambda/100$ integrated with an ENG spherical shell was introduced as shown in Fig. 4.1 (b). It was proved theoretically [43] and using HFSS simulations [42] that this system can be matched to the $50\ \Omega$ source without any external circuit. This means that ENG shell behaves as an inductor which cancels out the huge capacitance of the electric monopole. This approach was called metamaterial based antennas. The same procedure can be done to match a

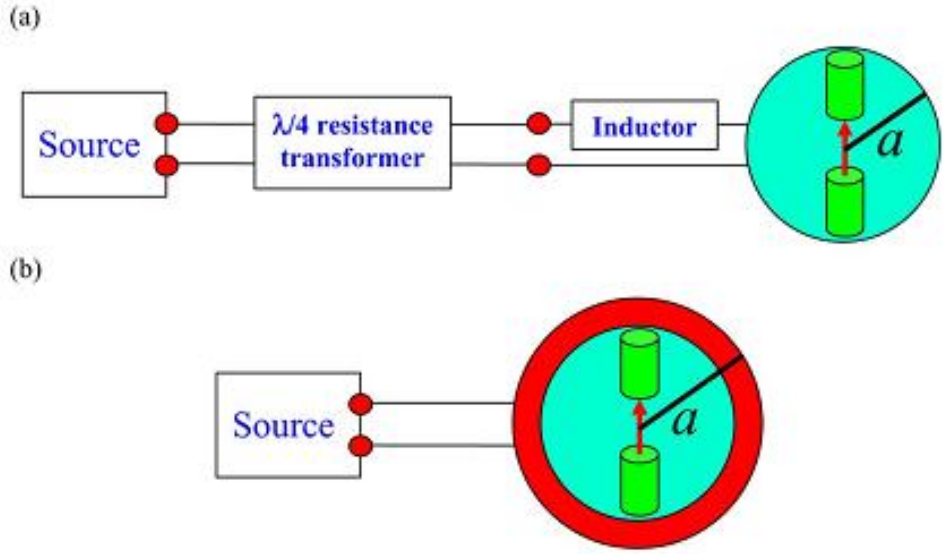

Figure 4.1: (a) Traditional method to match electrically small dipole using inductor to achieve reactance resonance then a λ/4 transmission line to match the resistive part to the source. (b) Electrically small electric dipole with an ENG shell is naturally matched to the source [45].

magnetic dipole by integrating it with a MNG shell which behaves as a capacitor. The whole system composed of the electric dipole and the ENG shell had $kr_e = 0.118$. Therefore, it is electrically small. Later in [44], a generalization was done for a multilayer system as shown in Fig. 4.2 (a). An optimization technique was used to maximize the far field radiated power. The optimization parameters were the shell radius and the medium parameters (ε, μ).

To prove that the radiation resistance is matched to the $50\ \Omega$ source, a system composed of an electric monopole fed by a $50\ \Omega$ coaxial cable and integrated with five metamaterial shells was studied as shown in Fig. 4.2 (b). The first and the last shells were air. The second and the fourth shells were glass (DPS[7] material). The third shell was filled with cold plasma (ENG material) with $\varepsilon_r = -10$. The

[7] DPS is abbreviation for double positive material (the usual material).

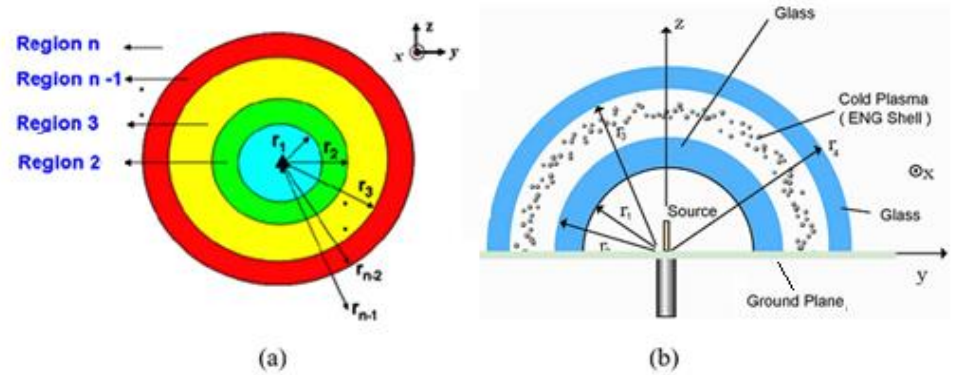

Figure 4.2: (a) An electrically small dipole-multilayered metamaterial shell system. (b) Coax-fed monopole-glass-ENG-glass shell system [44].

thickness of the ENG shell was optimized to achieve the maximum radiated power.

4.3 3D Physical Realizations

In order to make the design more practical, the spherical shell was replaced by placing a unit cell in the very near field of the antenna. Although this unit cell is not metamaterial by itself, its effect is similar to the ENG (MNG) shells discussed before. Thus, this antenna was called metamaterial inspired antenna.

3D realizations for metamaterial inspired ESAs are listed. These antennas are easy to design and fabricate, hence, they are often called easy (EZ) antennas. EZ antennas could be magnetic or electric based. An example for each type is listed below.

4.3.1 Magnetic-Based EZ Antenna System

In [45], a magnetic monopole was loaded with a capacitive loaded loop (CLL) unit cell as shown in Fig. 4.3 (a). The time varying magnetic flux generated by the time varying current in the electrically small magnetic monopole antenna is captured by the CLL surface. Large electric field will be generated between the

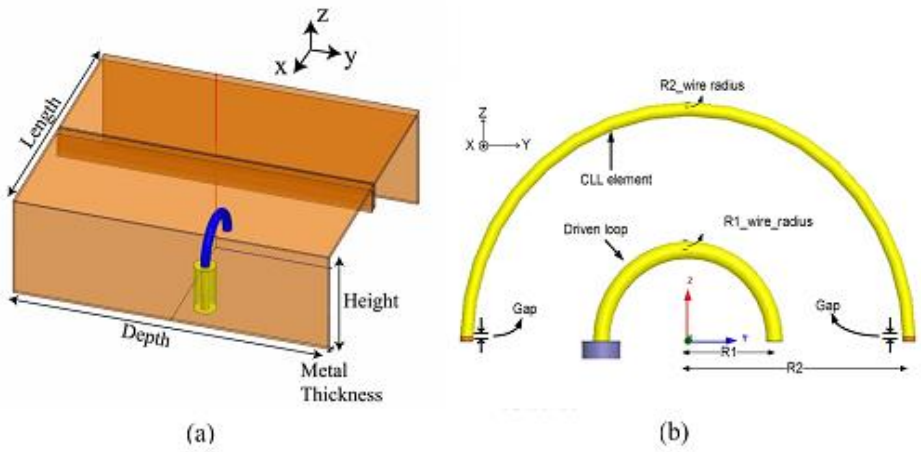

Figure 4.3: (a) Magnetic monopole antenna (magnetic monopole) is loaded with CLL unit cell [45]. (b) The same antenna is loaded with a split thick wire [46].

stub arms which has the effect of a very large capacitor. This capacitance matches the inductance due to the semi-loop antenna and the CLL surface. The entire system obeyed (4.2), hence, it is electrically small[8].

A simplification was done by replacing the CLL element with a split thick wire, as shown in Fig. 4.3 (b) [46]. This design has lower Q (higher BW) as it occupies the volume of the minimum enclosing sphere more efficiently. The electric field generated across the gaps which are filled with quartz provides the capacitance needed to match the antenna. Best magnetic coupling occurs when the magnetic monopole antenna and the wire are in the same plane. As the plane of the wire is rotated, it captures less magnetic flux. When the angle between the two planes (the wire and the magnetic monopole antenna) is 90^o, all incident power will be reflected and there will be no magnetic coupling.

[8] All antennas in this chapter are electrically small. Thus, we will not mention (4.1) and (4.2) anymore.

4.3.2 Electric-Based EZ Antenna System

These systems are dual to the magnetic based systems discussed in the previous section. In [45], an electric monopole was surrounded by a unit cell composed of a 3D cylindrical helical metal strip, as shown Fig. 4.4 (a). This unit cell captures the time varying electric field generated by the electric monopole. Induced current is generated in the metal strip which creates the inductance needed to match the antenna system.

Another EZ-electric based antenna called stub antenna was proposed in [47]. The principle of operation is to achieve the inductance needed to match the capacitive reactance of the antenna by placing a parasitic element composed of a stub connected to a lumped inductor in the very near field of the antenna, as shown in Fig. 4.4 (b). To get the lowest Q (highest BW), the volume within the radian sphere should be fully utilized by the antenna. Therefore, more than one parasitic element was used. Although the BW was enlarged, larger inductors were needed to achieve the same resonance frequency, as these inductors can be considered as a parallel combination. A more efficient way was proposed in [48] by adding a spherical part as shown in Fig. 4.4 (c). This antenna is called the canopy antenna and had lower Q (higher BW) than the other two antennas.

4.4 2D Physical Realizations

The purpose of 3D realizations was to prove the concept. 2D realizations were implemented by replacing the 3D unit cells with their equivalent 2D structures.

4.4.1 Magnetic-Based 2D EZ Antenna System

A 2D planer version of the magnetic-based EZ antenna was achieved by replacing the CLL element with an interdigitated capacitor, as shown in Fig. 4.5 (a) [45].

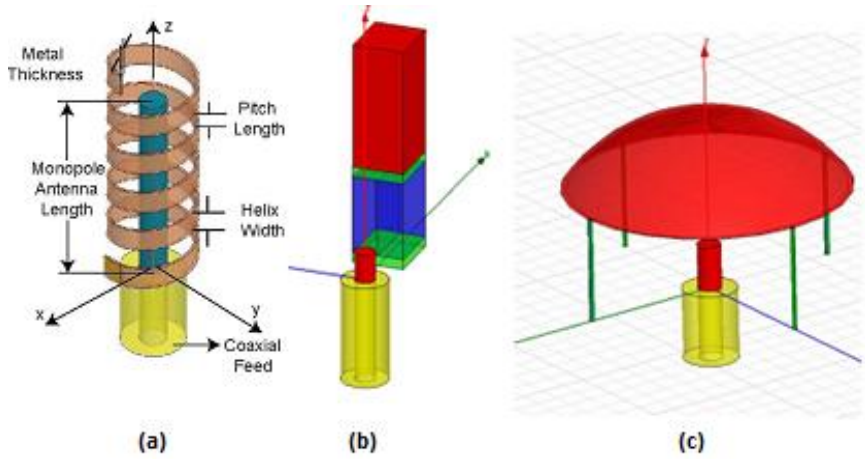

Figure 4.4: (a) Electric monopole loaded by a 3D cylindrical helical copper metal strip [44], (b) stub antenna [47], and (c) canopy antenna [48].

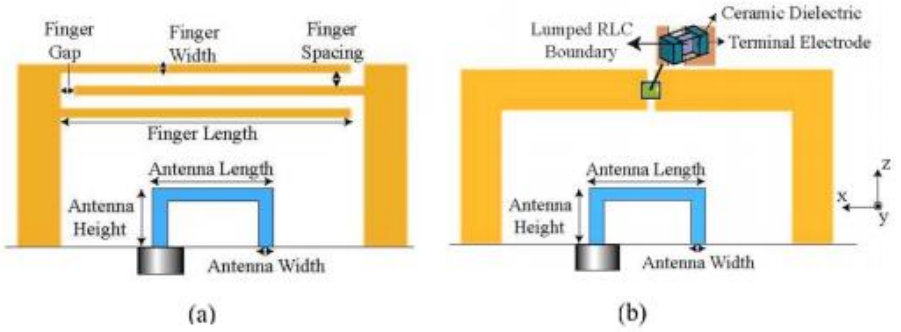

Figure 4.5: 2D version of the magnetic based EZ antenna system with CLL replaced by (a) an interdigitated capacitor, and (b) a lumped capacitor [45].

The region between the bottom interdigitated capacitor finger and the ground captures the time varying magnetic flux. Therefore, larger electric field will be generated between the interdigitated capacitor fingers providing enough capacitance to match the magnetic monopole antenna. Further simplification was done by replacing the interdigitated capacitor with a lumped capacitor, as shown in Fig. 4.5 (b). This antenna had better efficiency as conductor loss was decreased and it can be tuned easily.

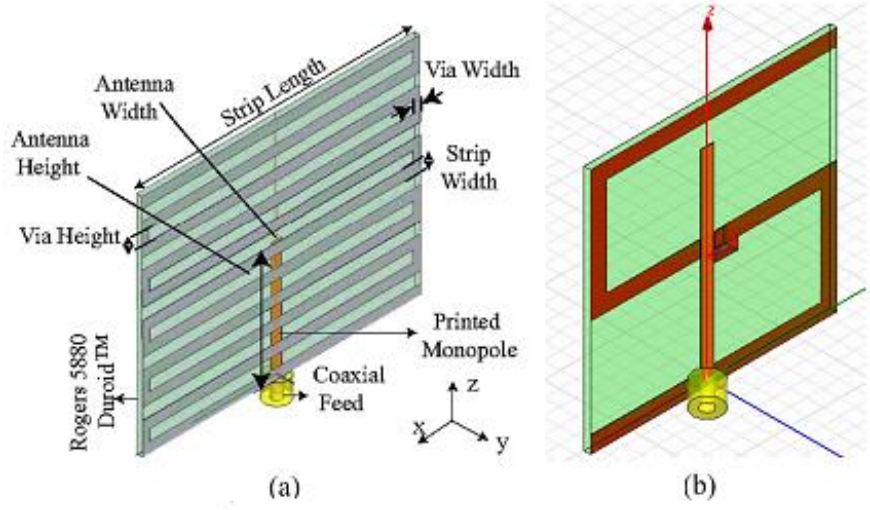

Figure 4.6: 2D version of the electric based EZ antenna system with the cylindrical helical copper metal strip replaced by (a) a meander line [45]. (b) 2 metal jaws with lumped inductor at the metal (Z-antenna) [48].

4.4.2 Electric-Based 2D EZ Antenna System

Same procedure was done to the electric-based EZ antenna shown in Fig. 4.4. A 2D version was achieved by replacing the cylindrical helical metal strip with a meander line, as shown in Fig. 4.6 (a) [45]. Although the same principle of operation can be applied here, the meander line can be treated as a series transmission lines (TLs), each one is terminated with short circuit. Therefore, it acts as group of inductors connected in series and matches the monopole capacitance. Further simplification was done in [48] by replacing the meander line with a Z-shaped conductor with a lumped inductor mounted on its center, as shown in Fig. 4.6 (b). This antenna has higher efficiency and can be tuned easily and called Z-antenna.

4.5 NFRP Element Loaded Antennas

To make the designing procedure straight forward, standard elements (electric or magnetic monopoles) were used to excite near field resonant parasitic (NFRP) elements inspired by the metamaterial unit cells. These NFRP elements can be electrically or magnetically coupled and there dimensions are optimized to achieve complete matching to the source.

Fig. 4.7 shows electric and magnetic monopoles used to excite NFRP elements. If the electric monopole is placed in the center of the NFRP element as shown in Fig. 4.7 (a), the total magnetic flux crossing the plane of the element is zero. Therefore it is electrically coupled. The same concept can be applied to Fig. 4.7 (b) where the magnetic flux is parallel to the element plane. Both elements in Fig. 4.7 (c), (d) are magnetically coupled as they are excited by magnetic flux. In the four systems shown in Fig. 4.7, magnetic resonance[9] is excited either electrically or magnetically. Two antennas were designed using the last concept. In Fig. 4.8 (a), an electric monopole was used to electrically excite a protractor shape NFRP. A gap was introduced to this design to add an extra degree of freedom to tune the antenna. This antenna was called a protractor antenna and operates in the magnetic resonance mode. In Fig. 4.8 (b), an electric dipole with curved top loadings (blue) was used to electrically excite a NFRP element (NFRP had the same shape (red) to increase the coupling). This antenna was called Egyptian axe antenna and operates in an electric resonance mode as the straight part of the NFRP element is the main radiator. To prove that the NFRP element is necessary to achieve matching, a simulation was done for a directly driven dipole without the parasitic element and for a directly driven

[9] Magnetic resonance means generation of a loop mode. On the other hand, electric resonance means generation of an electric dipole mode [49]

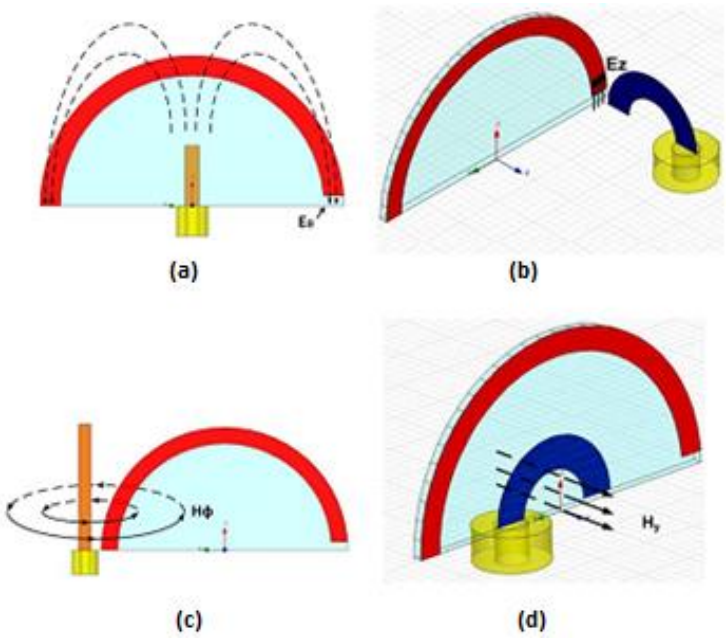

Figure 4.7: Electric and magnetic monopoles used to excite NFRP element either electrically or magnetically [49].

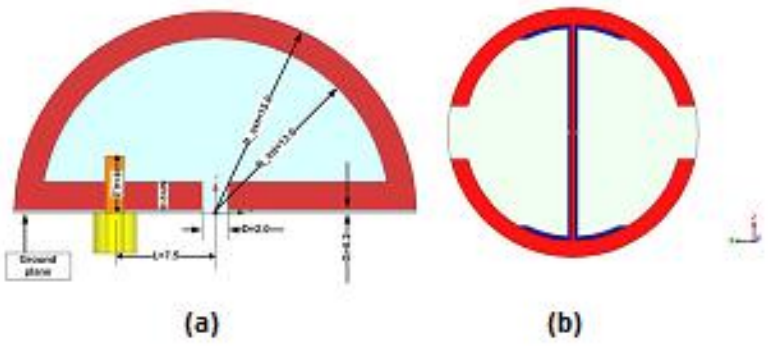

Figure 4.8: (a) Protractor antenna [49]. (b) Egyptian axe antenna [55].

parasitic dipole. It was found that no resonance occurs for the first case and very bad matching in the second case.

4.6 Applications

Metamaterial inspired ESAs are used in many applications due to their small size and high efficiency. Some applications for the antenna discussed in previous sections are listed here.

4.6.1 Dual-Band

Many applications require dual-band antenna to cover more than one standard [46], [49]. Dual band operation was achieved using two CLL elements as shown in Fig. 4.9. The first design is the same as discussed in Fig. 4.3 (b). As the two CLL elements have different lengths, they resonate at different frequencies. The lower (higher) frequency is due to the longer (shorter) CLL. It is expected that these frequencies will change because of the coupling between the two elements. At lower (higher) frequency currents in the two CLL elements are in-phase (out-of-phase). Therefore, they act as two capacitors in parallel (series). To make these two frequencies independent of each other, each CLL element is rotated with respect to the magnetic monopole antenna. As the angle between them increases, the coupling decreases till they are totally independent when the angle is 90o as shown in Fig. 4.9 (a). The same concept was applied to the protractor antenna shown in Fig. 4.9 (b) to achieve dual band operation. The only difference is that two printed monopoles were driven using a rectangular conductor.

4.6.2 Frequency-Notched UWB Antenna

Many UWB antennas require having a notch at certain frequencies to minimize electromagnetic interference (EMI) to other standards within their band. In [50], an UWB antenna was design using printed monopole antenna to cover the frequency range $3.1 - 10.6\ GHz$. A notched in the band was achieved by placing a CLL element near the feed line as shown in Fig. 4.10 (a). This CLL element is strongly coupled to the feed line, hence, it captures and stores all input energy at

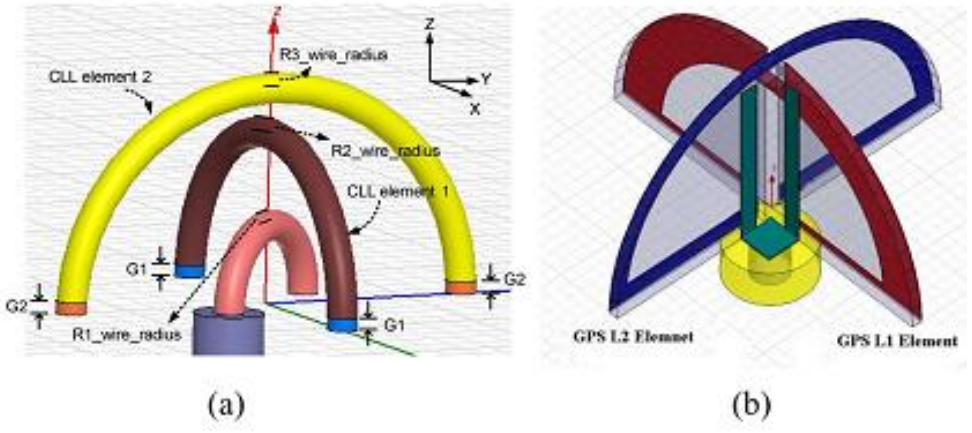

Figure 4.9: Dual band operation was achieved using: (a) two split thick wires [45], and (b) two protractor antennas [49].

its resonance frequency. This notched frequency was easily adjusted by modifying the gap of the CLL element. The band of the notched frequency could be modified by adjusting the location of the CLL element. To dual-band notched UWB antenna, two CLL elements were used as shown in Fig. 4.10 (b). It was found that these two elements are almost independent on each other. The same procedure can be used to design tri-band notched UWB antenna. As there is no enough space to put three CLL elements near the feed line, they should be resized to adjust the three notched frequencies. An alternative approach to get the tri-band is to adjust the CLL element in the top layer to for the lower rejection band and adjust the two CLL elements to reject the other two bands.

4.6.3 Circular Polarized Antenna

Circular polarization is an important feature in some applications. There are two types of circular polarized antenna [46]. The first type uses a superposition of two orthogonal electric (magnetic) dipoles driven in a phase quadrature. The second type uses a superposition of two collinear electric and magnetic dipoles.

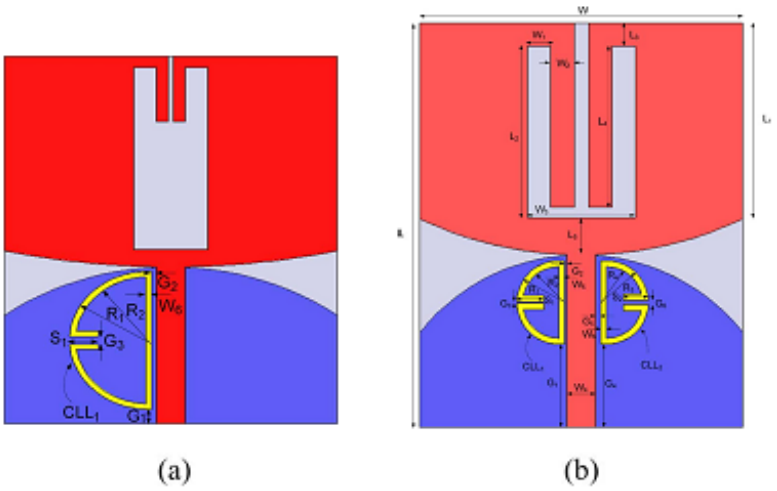

Figure 4.10: (a) Dual-notched UWB antenna using one element. (b) Tri-notched UWB antenna using two elements [50].

The structure shown in Fig. 4.9 (a) was used to achieve circular polarization as it is composed of two orthogonal magnetic dipoles. To get the phase quadrature, one CLL element was designed to work on its resonance mode and the other one was designed to work on its anti-resonance mode. As the CLL elements were designed to make these modes close to each other, the $\pi/2$ phase difference was achieved.

4.6.4 GPS Rectenna

Rectifying antennas (Rectenna) are used in power harvesting and wireless power transmission. In [51], a protractor antenna was used to implement a rectenna that operates at 1.57 GHz. To match the input impedance of the rectifying circuit, the gap, CLL width and patch width were adjusted as shown in Fig. 4.11.

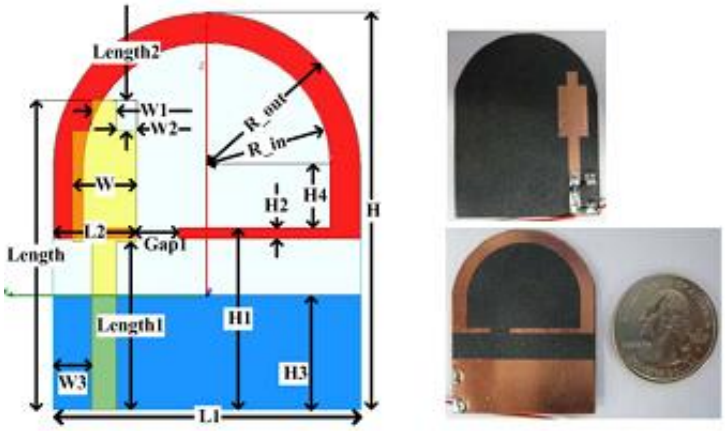

Figure 4.11: Protractor antenna with the rectifying circuit [51].

4.6.5 Active metamaterial Inspired Wideband ESA

In order to bring the antenna into resonance over a wide frequency range, non-Foster (NF) matching networks are required to realize negative inductances and capacitances [52].

This concept was first applied to the Z antenna in [53]. The antenna was treated as a two port network loaded with an inductor for reactance matching at certain frequency. To get this reactance matching over a wide BW, the inductor was replaced with a general matching network, as shown in Fig. 4.12, which had the following $ABCD$ matrix:

$$\begin{bmatrix} A_{Net} & B_{Net} \\ C_{Net} & D_{Net} \end{bmatrix} = \begin{bmatrix} A_{antenna} & B_{antenna} \\ C_{antenna} & D_{antenna} \end{bmatrix}^{-1} \begin{bmatrix} 1 & Z_s \\ 0 & 1 \end{bmatrix} \tag{4.5}$$

where Z_s is the source impedance. The input impedance for this matching network $Z_{Net} = B_{Net}/D_{Net}$ was found to be pure imaginary for the whole frequency range. Thus, this matching network could be implemented using

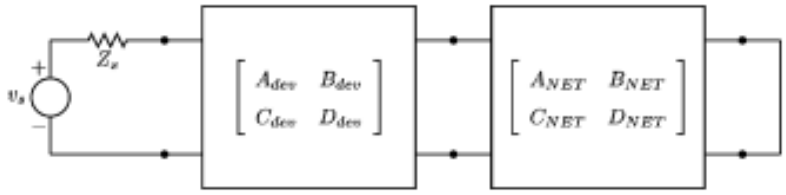

Figure 4.12: Antenna circuit model with the matching network [53].

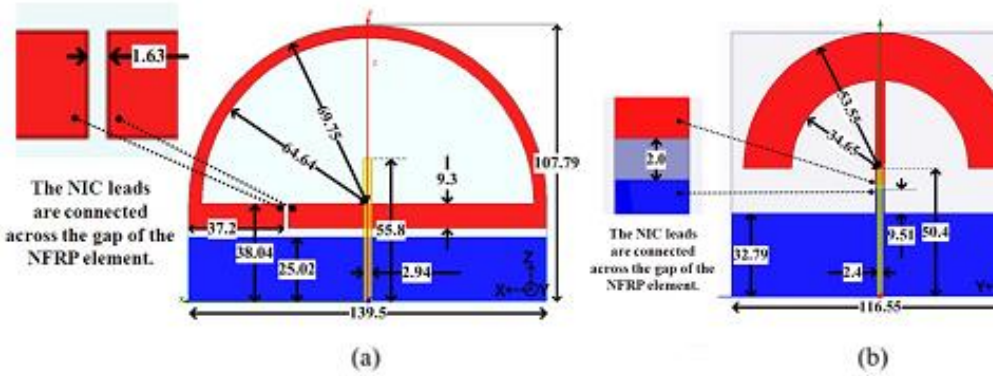

Figure 4.13: NIC used (a) with protractor antenna, and (b) with Egyptian axe antenna to achieve large BW [54].

frequency independent inductor. Twenty four inductors were used to bring the antenna into resonance. Using curve fitting, the values of these inductors were found to be inversely proportional with the frequency squared. It is obvious that foster reactance cannot achieve that behavior.

In [54], both protractor and Egyptian axe were designed to have large BW using a NF circuit. A negative impedance converter (NIC) was placed in both antennas as shown in Fig. 4.13.

4.7 Conclusion

This chapter outlined one of the most powerful techniques used to minimize the size of the antenna. It started with enclosing the antenna with a metamaterial spherical shell. Then, this shell was replaced by a unit cell (parasitic element) in the very near field of the antenna. Using this approach, ESAs were achieved. Some applications were mentioned to explain the physical concept of having an element coupled with the antenna.

The concept of metamaterial inspired ESAs will be used in the next chapter to design a novel compact size DVB-H antenna.

Chapter 5
N-Internal Port Design for Wideband Electrically Small Antennas

Metamaterial concept was used to reduce the size of the antenna using two approaches: metamaterial based/inspired ESAs, as was shown in the previous chapter. The second approach is similar to the well-known trap antennas [39], especially when the reactance element is directly coupled to the antennas.

In this chapter, a study of the maximum bandwidth that can be achieved using the second approach is conducted and, as an application, a novel compact-size DVB-H antenna is proposed. Lumped elements are used for two reasons. First of all, they can be modeled as internal ports with the size independent of the element's value[10]. Thus, makes it possible to build a model. Second, they are available with very large values, which may significantly reduce the electrical length of the antenna.

[10] For the same lumped element family, all values have the same package size.

To our knowledge, no closed form solution was developed to predict exactly the effect of the lumped elements on the antenna's bandwidth. Although this may be considered as an optimization problem, finding a closed form solution will help to better understand the behavior of the antenna. Another important benefit of the proposed model is to know exactly the boundary of the solution (without excessive EM simulations). Thus, simulation time will be significantly reduced, especially if there is more than one lumped element.

This chapter begins with a brief description for the work that inspired us to come up with the model. Then, network theory [26] is used to explain how to deal with n-lumped elements connected to an antenna. An illustrative example on how to use this model for the case of 1-internal port antenna will be discussed. Finally, an electrically small DVB-H antenna will be implemented using the proposed model.

5.1 Previous Work

The Z-antenna presented in [53] was a good example to demonstrate how an electric monopole can radiate at lower frequencies by using the metamaterial inspired concept (i.e. by indirectly loading it with a large inductor in its very near field).

In [56], it was shown that an electric dipole can be equivalent to this Z-antenna by folding, meandering and inductive loading it. The claim was that an electric dipole, which can be represented by an RLC circuit, keeps radiating as long as its input impedance is matched to the $50\,\Omega$ feeding source. Folding process will not change the resonance frequency (as long as there is no full current cancelation), yet, its capacitive reactance will increase. An inductance is then added to one arm to lower the radiation frequency. This arm is then optimized to match the resistive part of the input impedance and also to minimize

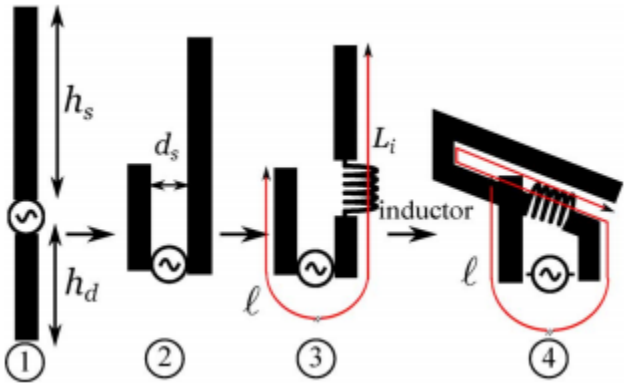

(a)

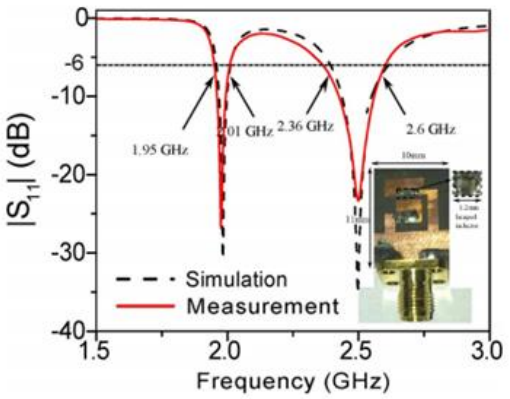

(b)

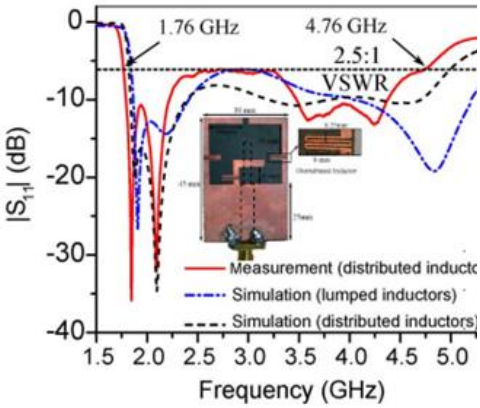

(c)

Figure 5.1: (a) Folding, loading and meandering an asymmetric electric dipole. (b) Dual-band operation. (c) Wideband operation [56].

the size. These steps are shown in Fig. 5.1 (a). An application for this explanation was to design an electrically small dual-band antenna, as shown in Fig. 5.1 (b). Wideband operation was also achieved by staggering multiple resonance frequencies together as shown in Fig. 5.1 (c).

Now, one may ask the following questions: are all these steps really needed? What is the maximum bandwidth that can be achieved using a single-arm electric dipole antenna? Why are the bands separated for some inductance values, and staggered for others? How does an antenna behave when loading it with inductance/ capacitance (without doing excessive EM simulations)? These questions can be answered using the model proposed in next sections.

5.2 N-Internal Port Antennas

In [53], an antenna with one lumped element was modeled using *ABCD* parameters. Such a model has two main problems. First, $ABCD$ parameters cannot model more than one lumped element, as they cannot be considered as cascaded blocks. Second, that model explained how to achieve perfect matching (i.e. $50\ \Omega$ resistance with zero reactance). However, it did not predict the wideband performance that an antenna with such a lumped element could achieve. In this section, a generalized model is proposed.

In general, antennas with n-lumped elements can be considered as n+1 port network (1-feeding port and n-internal ports) as shown in Fig. 5.2. The corresponding Z-parameters model in matrix form is:

$$\begin{bmatrix} v_1 \\ \vdots \\ v_{n+1} \end{bmatrix} = \begin{bmatrix} Z_{1,1} & \cdots & Z_{1+n} \\ \vdots & \ddots & \vdots \\ Z_{n+1,1} & \cdots & Z_{n+1,n+1} \end{bmatrix} \begin{bmatrix} i_1 \\ \vdots \\ i_{n+1} \end{bmatrix} \tag{5.1}$$

where $v_1, \dots, v_{n+1}$ and $i_1, \dots, i_{n+1}$ are voltages and currents at each port with directions shown in Fig. 5.2. On the other hand, lumped elements are considered as boundary conditions on the internal ports with the following expressions

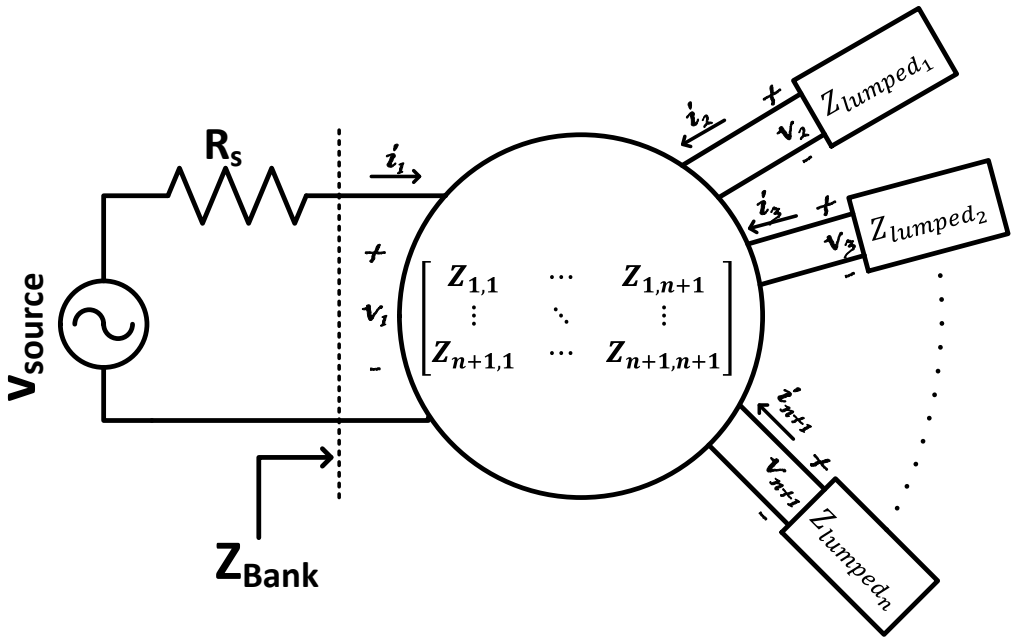

Figure 5.2: Model of an antenna with n-internal ports using Z-parameters. Z_{Bank} are the input impedance values that will match the system to the right of the dashed line to R_s with $C\ dB$ reflection coefficient.

$$Z_{lumped,k} = -\frac{v_{k+1}}{i_{k+1}} \qquad : k = 1, 2, \cdots, n \tag{5.2}$$

To know exactly the bandwidth of the new system (the antenna with n-lumped elements), Z_{Bank} is defined as a bank of all impedance values that will cause the reflection coefficient ($|S_{11}|$) to be lower than certain dB level (C) when connected to a source with input resistance (R_s). Thus,

$$20\log(|S_{11}|) \leq C \tag{5.3}$$

where,

$$|S_{11}| = \left|\frac{Z_{Bank} - R_s}{Z_{Bank} + R_s}\right| \qquad : Z_{Bank} = R + jX$$

After some mathematical manipulations, it can be shown that

$$(R - R_o)^2 + X^2 \leq a^2 \tag{5.4}$$

where,

$$R_o = R_s\left(\frac{1+k^2}{1-k^2}\right) \qquad : a = \frac{2R_s k}{1-k^2}\,, k = 10^{c/20}$$

This means that Z_{Bank} is a disk in the complex plane with its center at $(R_o, 0)$ and radius a. At each frequency, having $v_1/i_1 \in Z_{Bank}$ means that Z_{lumped} is a solution for the system in Fig. 5.2, i.e. Z_{Bank} itself is a boundary condition, which when combined with (5.2) gives the following diagonal boundary condition matrix:

$$\begin{bmatrix} v_1 \\ v_2 \\ \vdots \\ v_{n+1} \end{bmatrix} = \begin{bmatrix} Z_{Bank} & 0 & \cdots & 0 \\ 0 & -Z_{lumped_1} & \cdots & 0 \\ \vdots & \vdots & \ddots & \vdots \\ 0 & 0 & \cdots & -Z_{lumped_n} \end{bmatrix} \begin{bmatrix} i_1 \\ i_2 \\ \vdots \\ i_{n+1} \end{bmatrix} \tag{5.5}$$

Equations (5.1) and (5.5) are solved together to give the following $n+1$ system of equations:

$$\begin{bmatrix} Z_{11} - Z_{Bank} & Z_{1,2} & \cdots & Z_{1,n+1} \\ Z_{2,1} & Z_{2,2} + Z_{lumped_1} & \cdots & Z_{2,n+1} \\ \vdots & \vdots & \ddots & \vdots \\ Z_{n+1,1} & Z_{n+1,2} & \cdots & Z_{n+1,n+1} + Z_{lumped_n} \end{bmatrix} \begin{bmatrix} i_1 \\ i_2 \\ \vdots \\ i_{n+1} \end{bmatrix} = 0 \tag{5.6}$$

This system has $2n+1$ dimensions: frequency, $Re(Z_{lumped})$ and $Im(Z_{lumped})$. It reduces to $n+1$ dimensions for the case of lossless Z_{lumped}. To have a non-trivial solution, the determinant of the coefficient matrix must equal

zero. The solution of this determinant equation gives all Z_{lumped} values that would match the antenna to C dB or below.

5.3 Illustrative Example: Antenna with One-Internal Port

An application for the model discussed in the previous section is to examine the maximum bandwidth that can be achieved using one lumped element. The host antenna is the well-established printed dipole antenna because it has omni-directional radiation pattern. Nevertheless, the model can be extended to whatever host antenna.

Fig. 5.3 shows a conventional printed dipole antenna designed on Rogers 5870 with substrate thickness of 1.57 mm and a relative dielectric constant (ε_r) of 2.33. Simulations are carried out on HFSS $V.13.0$ [57]. This dipole is loaded with 1-lumped element on its bottom side arm to achieve a matching level of at least $-6\ dB$ ($C = -6$ in (5.3)). The size of the lumped port is determined based on the actual lumped element size. As 0603 package ($1.6 \times 0.8\ mm^2$) [58] will be used, lumped-port size is chosen to be $1 \times 1\ mm^2$ (to allow soldering). Since this antenna has only 1-internal port ($n = 1$), equation (5.6) will be:

$$\begin{bmatrix} Z_{1,1} - Z_{Bank} & Z_{1,2} \\ Z_{2,1} & Z_{2,2} + Z_{lumped} \end{bmatrix} \begin{bmatrix} i_1 \\ i_2 \end{bmatrix} = 0 \qquad (5.7)$$

Equating the determinant of the coefficient matrix to zero will result in the following equation

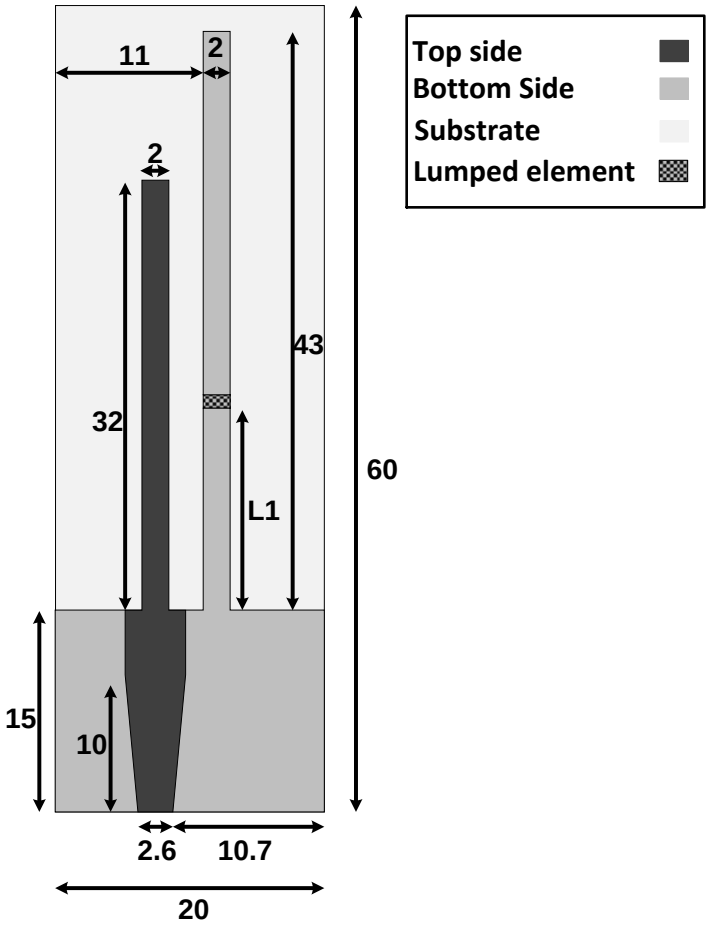

Figure 5.3: Structure of a printed dipole antenna loaded with one-lumped element. Dimensions are in mm.

$$Z_{lumped} = \frac{Z_{1,2}Z_{2,1}}{Z_{1,1} - Z_{Bank}} - Z_{2,2} \tag{5.8}$$

One should not forget that Z_{Bank} is a disk in the complex plane (5.4). Thus, $Z_{lumped} = R + jX$ has a solution that is also a surface in the complex plane. Since Z_{lumped} has to be pure imaginary (real values will consume power and hence degrades the efficiency), the practical solution is the intersection of Z_{lupmed}

surface with the imaginary axis. Equation (5.8) is a typical bilinear transformation [59]. This means that Z_{lupmed} is either a disk or an annulus as shown in Fig. 5.4. The gray region represents all Z_{lumped} values that cause a match of $-6\ dB$ or better at certain frequency. X_1 and X_2 represent the boundary of the practical solution (which is represented by the thick lines on the imaginary axis in Z_{lumped} plane).

To code up this method, Z-parameters are extracted from HFSS (as z2p file). At each frequency three points (P_1, P_2, and P_3) on the boundary of Z_{Bank} pass through (5.8) to get the equation of the outer (inner) circle in the case of disk (annulus) solution. This circle is defined by its center (r_o, x_o) and radius a' and has the following from

$$(R - r_o)^2 + (X - x_o)^2 = a^2 \qquad (5.9)$$

Since R is assumed to be zero hence, X_1 and X_2 are the solutions of a simple quadratic equation. One more point (P4) is chosen inside Z_{Bank} to pass through(5.8). This will indicate if $Z_{lumped} \in [X_1, X_2]$, or $Z_{lumped} \in (-\infty, X_1] \cup [X_2, \infty)$. Both cases are shown in Fig. 5.4 (a), (b), respectively.

Using MATLAB [60], the previous procedure is applied on the whole frequency range. This results in predicting X_1, X_2, and whether the solution is inside or outside them. Fig. 5.5 (a) shows the values of X_1 and X_2 for 0-5 GHz frequency range. It should be noted that X_1 and X_2 represent the boundary of the solution of the system of equations in (5.7). Each reactance value will result in matching the antenna over certain frequency range (with at least-6 dB matching level).

Fig. 5.5 (b) and (c) show the corresponding inductance and capacitance values, respectively.

The following remarks can be observed form Fig. 5.5:

1 Although both inductor and capacitors can be used to match the antenna, inductors result in much higher bandwidth for the printed dipole antenna.

2 Frequencies at which no match occurs, indicates that Z_{lumped} is a disk that does not intersect with the imaginary axis. Since the host antenna is responsible for the Z-parameters in (5.8), it can be said that each host antenna can support certain frequency range. This frequency range can be achieved by loading the antenna with lumped elements. Number, positions and values of these lumped elements are parameters that should be optimized.

3 Fig. 5.5 (b) shows that there is an optimum value of inductance that will cause maximum bandwidth. In this example, 17.7 nH will match the antenna over the frequency range from 1.05 GHz to 4.43 GHz. Simulated $|S_{11}|$ for both unloaded and loaded printed dipole is shown in Fig. 5.6.

4 Having zero inductance or infinite capacitance bring the antenna into the unloaded case as shown in Fig. 5.5 (a) and (b), respectively.

5 Open circuit can be considered as lumped element with infinite inductance.

6 Fig. 5.6 shows $|S_{11}|$ for the case of leaving the lumped port unconnected (microstrip gap with the same length of the lumped port), which is also predicted by Fig. 5. 5 (b).

7 The position of the lumped element is an important parameter. Fig. 5.7 shows the effect of the position of the lumped element on antenna's bandwidth. The maximum bandwidth is achieved when $L_1 = 15mm$. As

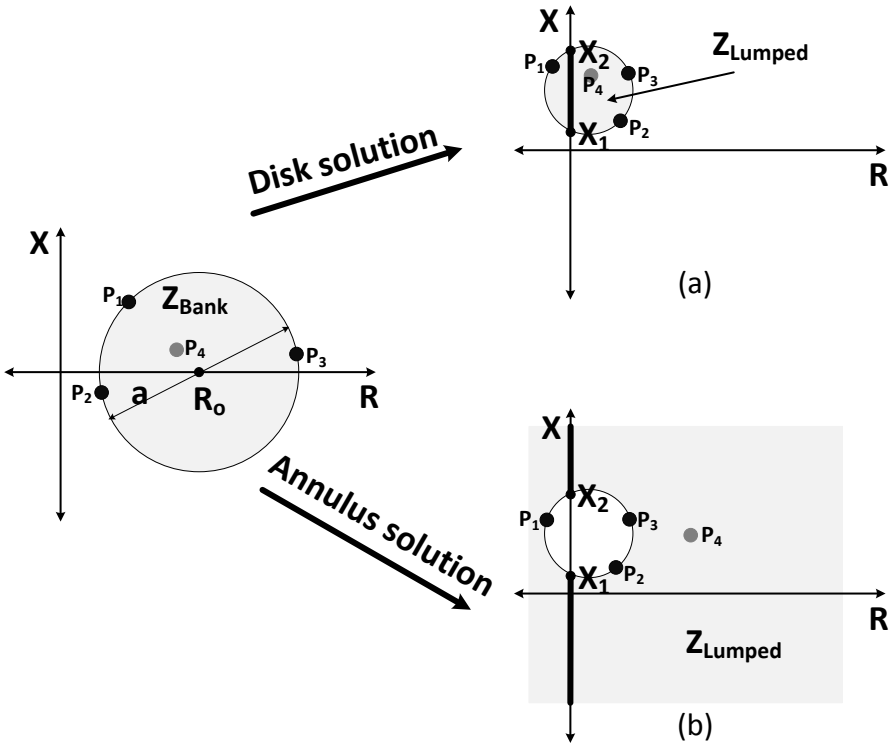

Figure 5.4: Transformation of Z_{Bank} disk to Z_{lumped} which is either: (a) disk or, (b) annulus. The thick line on the imaginary axis in Z_{lumped} plane represents all pure imaginary Z_{lumped} values that make $|S_{11}| \leq -6$ dB at a certain frequency. The three points (P_1, P_2, and P_3) are used to get the circle equation in (a) and (b). One more point (P_4) is used to know whether the solution is a disk or an annulus.

explained in [56], [61], components are placed around the position of maximum current (this position is found with respect to the unloaded antenna). An EM simulation should be run for each port position (then Z-parameters are extracted and imported into MATLAB).

It should be noted that after finding the optimum value using MATLAB, one more EM simulation has to be run (with the lumped element value instead of the lumped port) to find the antenna parameters (radiation efficiency and radiation pattern).

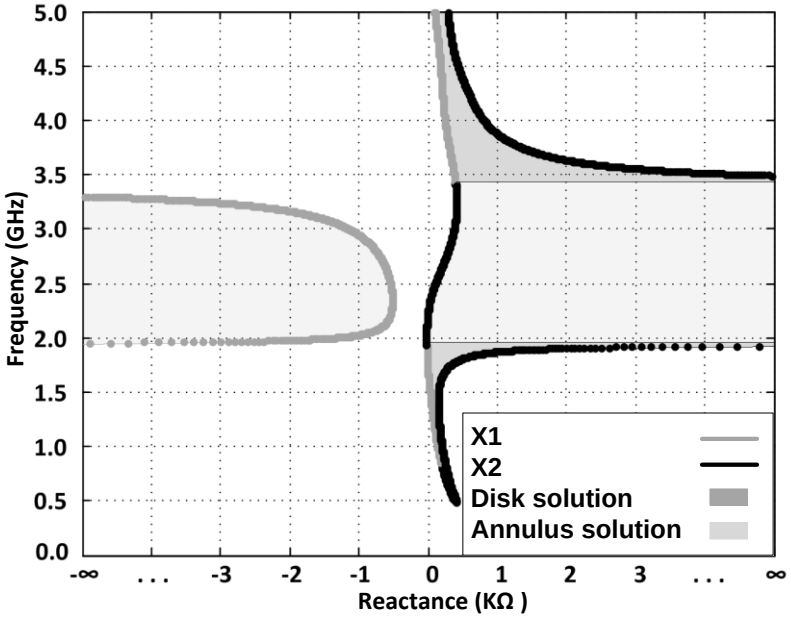
5.0
4.5
4.0
3.5
3.0
2.5
2.0
1.5
1.0
0.5
0.0
Frequency (GHz)
-∞ . . . -3 -2 -1 0 1 2 3 . . . ∞
Reactance (KΩ)
X1
X2
Disk solution
Annulus solution

(a)

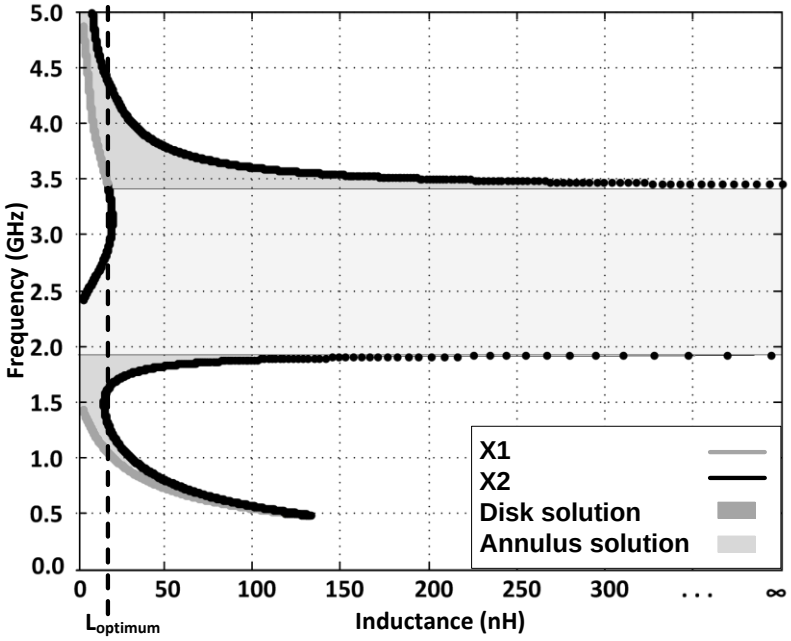
5.0
4.5
4.0
3.5
3.0
2.5
2.0
1.5
1.0
0.5
0.0
Frequency (GHz)
0 50 100 150 200 250 300 . . . ∞
L optimum
Inductance (nH)
X1
X2
Disk solution
Annulus solution

(b)

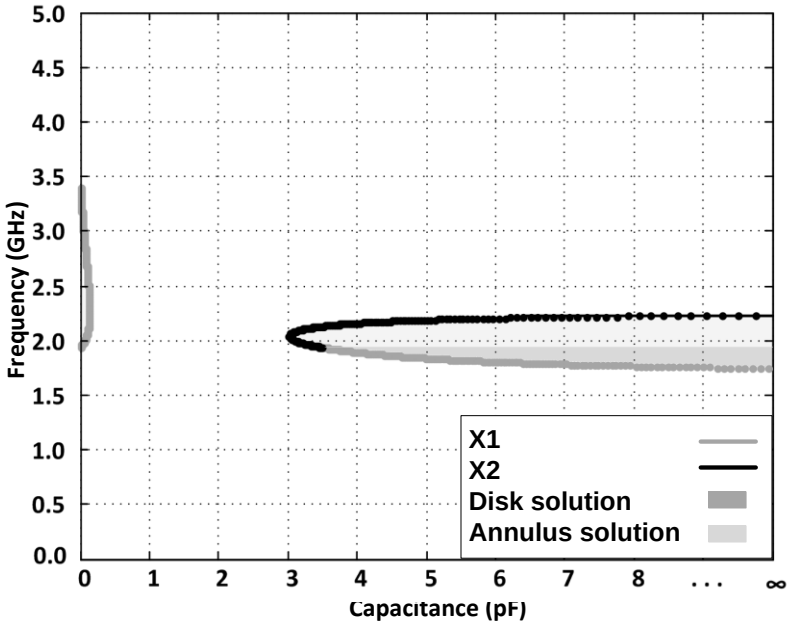

(c)

Figure 5.5: Solution to the system of equations (5.7) for $L_1 = 15mm$. X_1 and X_2 represent the boundary of the solution (i.e. each reactance value matches the antenna over the frequency range defined by X_1 and X_2). The red arrows define the frequency solution vs.: (a) Z_{lumped}, (b) inductance and (c) capacitance.

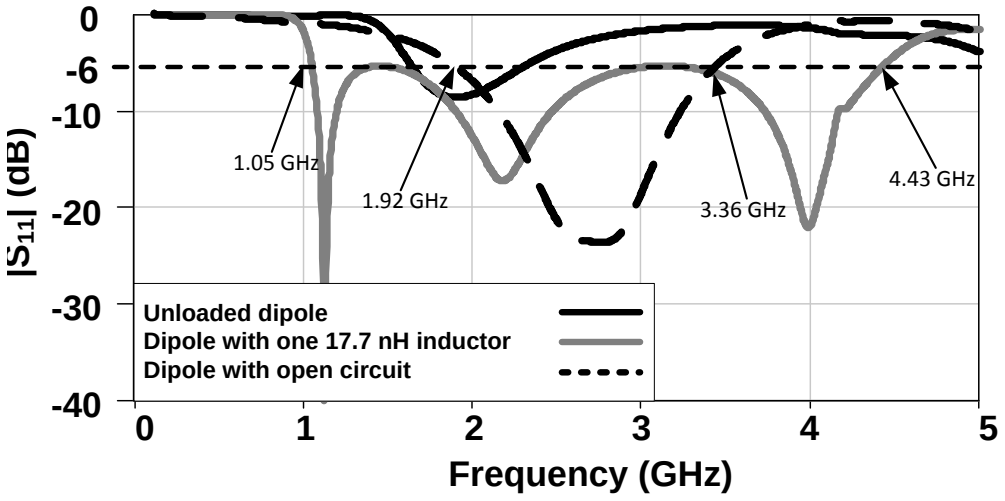

Figure 5.6: HFSS simulated $|S_{11}|$ for the unloaded and loaded printed dipole antenna (L_1=15mm).

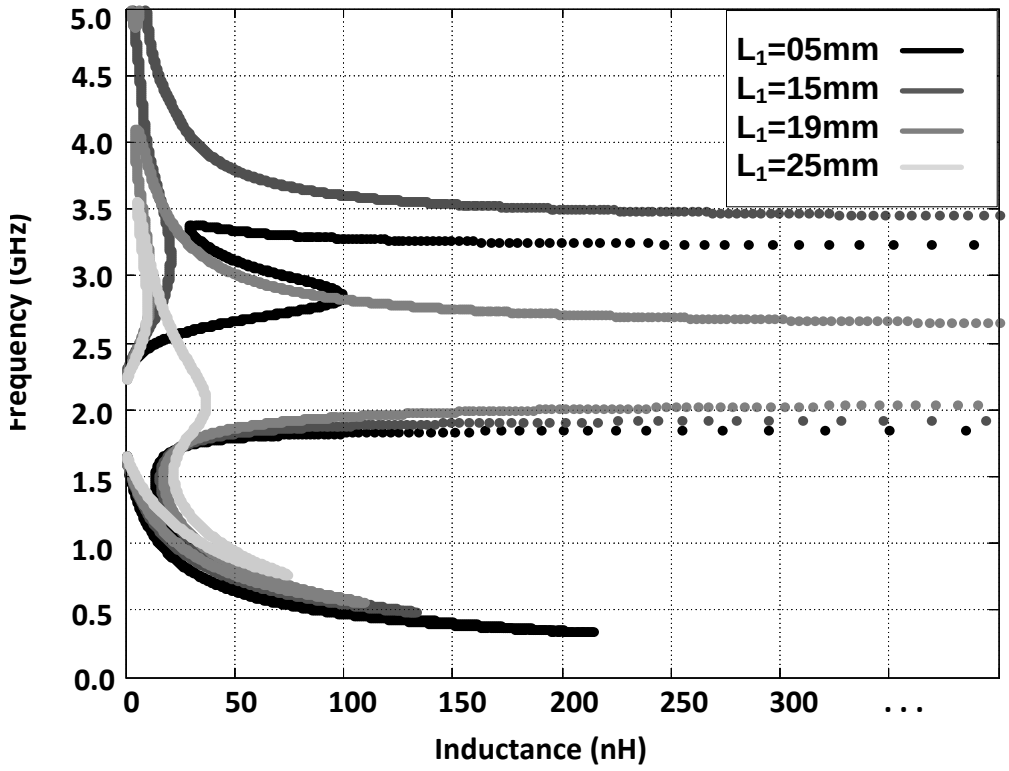

Figure 5.7: Frequency vs. inductance values for different lumped element locations (L_1 values).

To design a DVB-H antenna, single dipole is found to be not sufficient. To maintain the same size of the antenna, one more degree of freedom had to be added to the problem. This was achieved by printing another arm for the dipole and inserting a second lumped element, as will be discussed in the following section.

5.4 DVB-H Antenna with Two-Internal Ports

In this section, a 2-lumped element electrically small DVB-H antenna is proposed. Although more internal ports result in much complicated equations, it will be shown here that this model is very similar to the simple model discussed in the previous section.

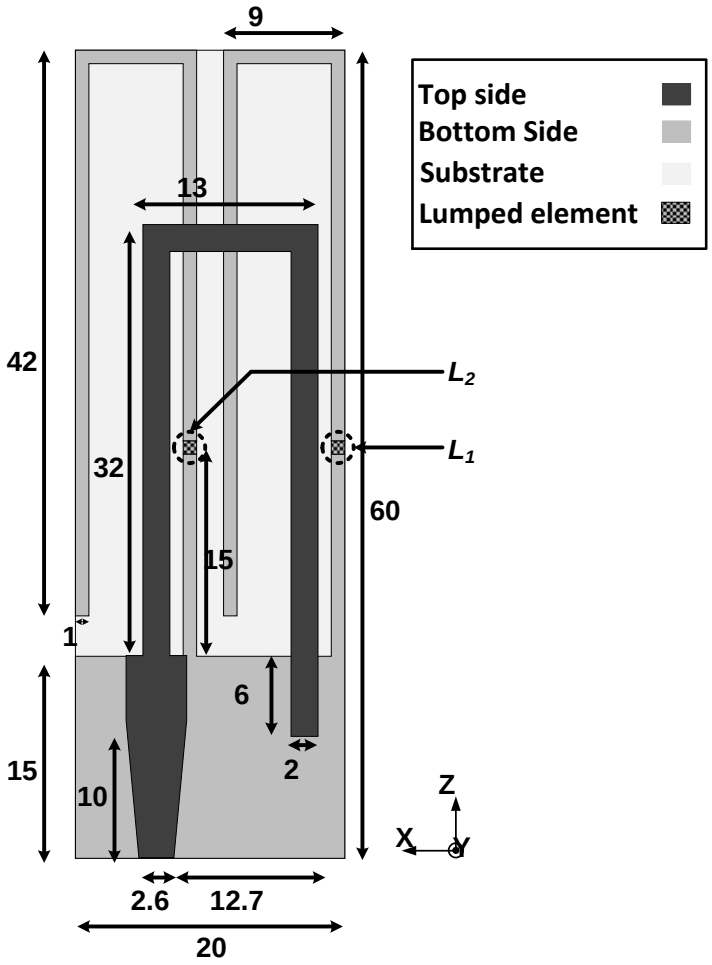

Figure 5.8: Structure of the proposed DVB-H antenna loaded with two-lumped element (shown in red with 1mm length). Dimensions are in mm.

Fig. 5.8 shows the proposed antenna. It is mainly a dipole antenna with one extra arm to increase the bandwidth. Similar to the previous example, this antenna is designed on Rogers 5870 with substrate thickness of 1.57 mm and a relative dielectric constant (ε_r) of 2.33 and it is loaded with 2-lumped elements on its bottom side arm to achieve a matching level of at least -6 dB ($C = -6$ in (5.3)). Again, substituting in (5.6) with n=2 results in the following system of equations:

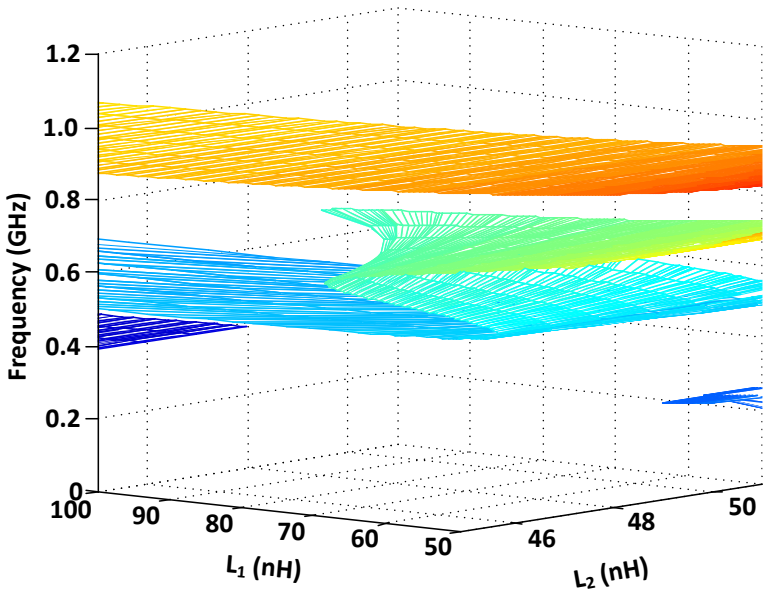

Figure 5.9: Solution to the system of equations (5.10) bounded by the two surfaces.

$$\begin{bmatrix} Z_{1,1} - Z_{Bank} & Z_{1,2} & Z_{1,3} \\ Z_{2,1} & Z_{2,2} + Z_{lumped_1} & Z_{2,3} \\ Z_{3,1} & Z_{3,2} & Z_{3,3} + Z_{lumped_2} \end{bmatrix} \begin{bmatrix} i_1 \\ i_2 \\ i_3 \end{bmatrix} = 0 \qquad (5.10)$$

Equating the determinant of the coefficient matrix to zero will result in the following equation

$$Z_{lumped_1} = \frac{BC}{Z_{lumped_2} - D} + A \qquad (5.11)$$

where,

$$A = \frac{Z_{1,2}Z_{2,1}}{Z_{1,1} - Z_{Bank}} - Z_{2,2}\ , \qquad B = \frac{Z_{2,1}Z_{1,3}}{Z_{1,1} - Z_{Bank}} - Z_{2,3}\ ,$$

$$C = \frac{Z_{3,1}Z_{1,2}}{Z_{1,1} - Z_{Bank}} - Z_{3,2}\ , \quad \text{and} \quad D = \frac{Z_{3,1}Z_{1,3}}{Z_{1,1} - Z_{Bank}} - Z_{3,3}$$

Equation (5.11) with its coefficients A,B,C and D has the same form as (5.8). Thus, it is a bilinear transformation. To know the boundary of the solution for the system of equations in (5.10) same procedure is followed (as in the previous section). The solution here is more difficult to be visualized as it will be a volume instead of a surface. As there are 2-lumped elements, four combinations of inductors and capacitors can be used to match the antenna. Using the algorithm presented above, it is found that two inductors result in higher bandwidth for this host structure. X_1 and X_2 are now surfaces instead of lines. Fig. 5.9 shows part of the solution for the case of two inductors (L_1, and L_2). Each combination of L_1 and L_2 results in matching the antenna over the frequency range defined by the two surfaces (with at least -6 dB matching level). Maximum bandwidth is achieved when L_1 and L_2 equal $120\ nH$ and $51\ nH$, respectively.

5.5 Antenna Measurements

5.5.1 Reflection Coefficient

The fabricated structure is shown in Fig. 5.10. Commercially available $0603HP$ RF inductors [58] are used. These inductors are placed around the position of maximum current for the unloaded case. It should be noted that the bend in the arms does not cancel the current significantly as the magnitude of the forward current is much larger than the backward one. This is due to the existence of the lumped inductors in the path of the forward current which makes its electrical length much longer than the backward current one.

S-parameter measurements are carried out on Rhode&Schwartz vector network analyzer (ZVB-14) Fig. 5.11 shows both simulated and measured $|S_{11}|$ for the proposed antenna. The antenna is matched over the DVB-H band ($470-855\ MHz$) which coincides precisely with the bandwidth calculated by the proposed algorithm. Fig. 5.11 also shows that the unloaded antenna does not have

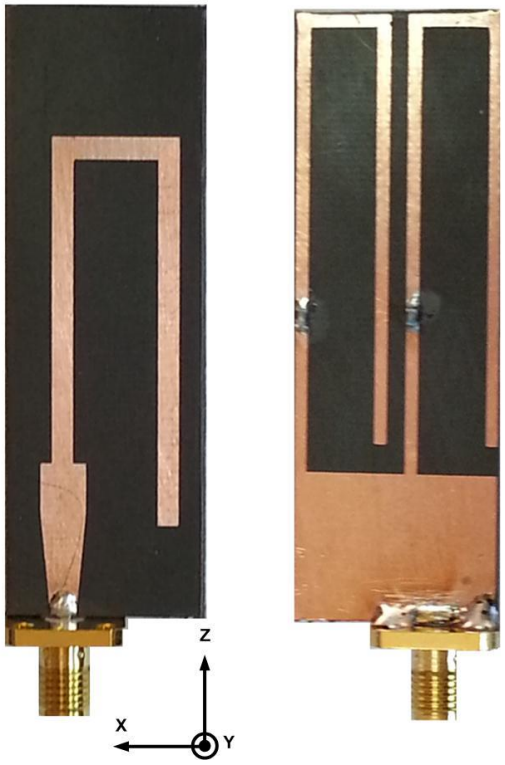

Figure 5.10: Fabricated structure (a) top layer, and (b) bottom layer.

any resonance in the DVB-H band. Since this antenna has a maximum dimension of 5 cm, then $kr_e < 0.5$ (k is the free space wave number and r_e is the radius of the smallest sphere enclosing the antenna). Thus, it is considered electrically small [62].

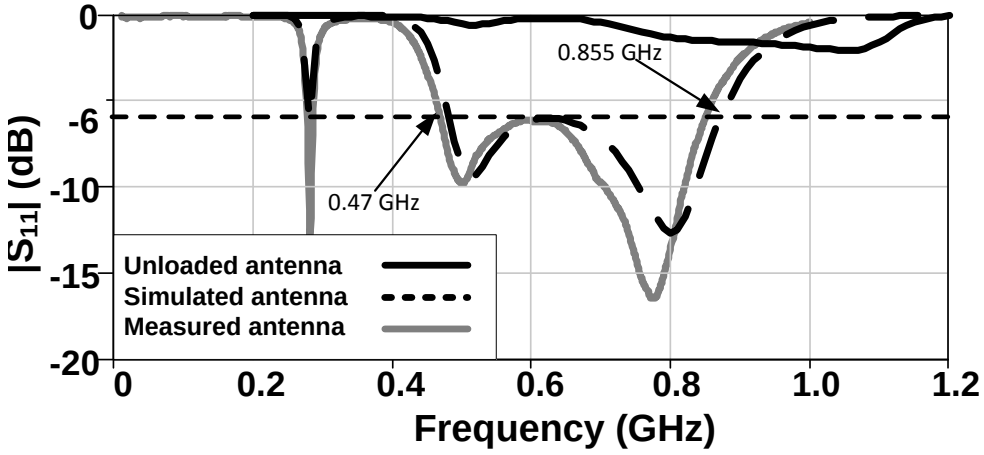

Figure 5.11: Simulated and measured $|S_{11}|$ for the proposed DVB-H antenna. The solid black line represents the simulated $|S_{11}|$ for the unloaded antenna.

5.5.2 Radiation Pattern and Efficiency

The radiation pattern was measured at free space using two identical antennas, as shown in Fig. 5.12. The distance between the two antennas was kept as small as possible to maximize the received power and in the same time ensures far-field measurements [32]. Fig. 5.13 shows the simulated and measured co-polarized radiation pattern at two frequencies, 500 MHz and 800 MHz. The antenna has an omnidirectional radiation pattern. The small asymmetry in the XZ-plan is due to the asymmetric current distribution indicated before. The cross-polarized radiation pattern could not be measured because of the very high radiation received from the surrounding devices (simulated cross-polarized radiation pattern is very weak as shown Fig. 5.13.

Efficiency is measured using different Wheeler-cap methods [35] - [38]. Table 5.1 shows the peak simulated and measured efficiencies within each band. Fluctuations between different Wheeler-cap methods are about 2%.

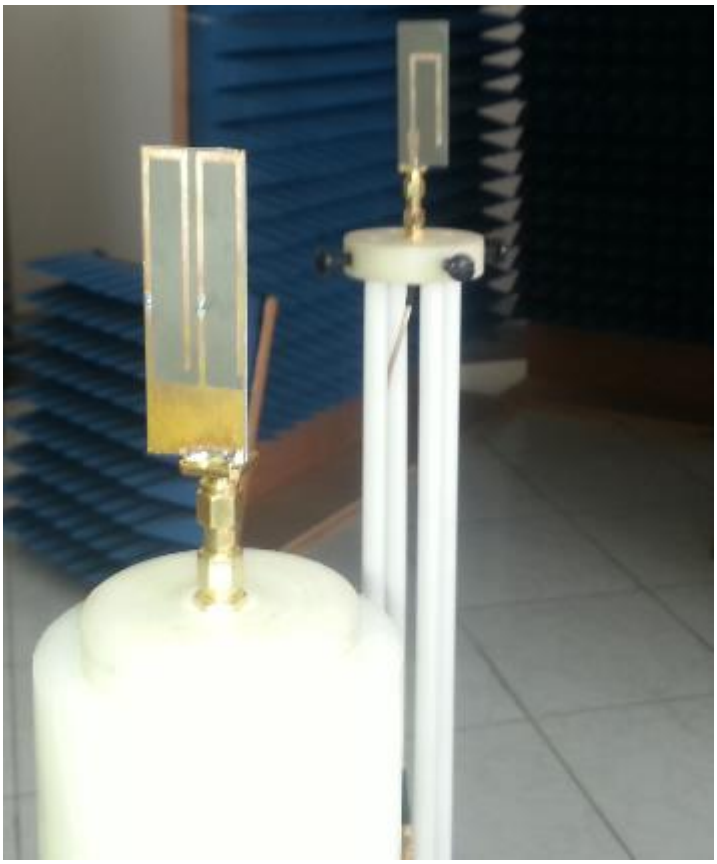

Figure 5.12: Two identical antennas were used in free space to measure the radiation pattern.

Table 5.1: Simulated and measured efficiency at two frequencies

Frequency (GHz)	Simulated efficiency (%)	Measured efficiency (%)
0.5	97	92
0.8	98	94

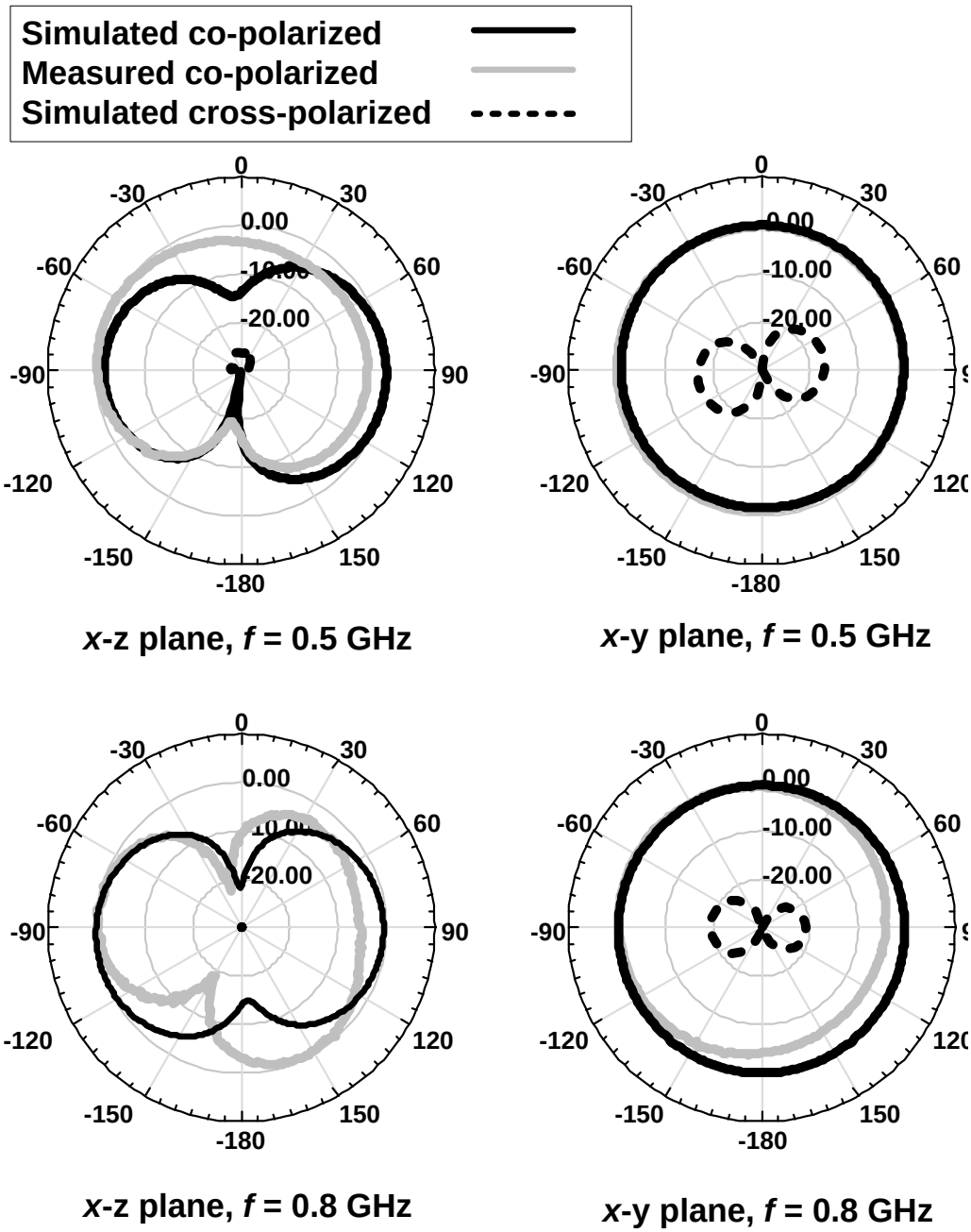

Figure 5.13: Simulated and measured normalized radiation patterns for the proposed antenna at two frequencies, on dB scale. Axis is shown in Fig. 5.10.

5.6 Conclusion

Antennas with n-lumped components were treated as antennas with n-internal ports. The new treatment set the boundaries of the lumped components values and permit the choice of commercial available values to realize wideband electrically small antennas without altering the radiation pattern and through simple, straight-forward, and time-saving algorithms.

Based on the proposed theory, a compact electrically small DVB-H antenna was proposed. The antenna has size of 2 cm ×5 cm, less than -6 dB reflection coefficient, omnidirectional radiation pattern, and more than 90% efficiency.

Chapter 6
Conclusion and Future Work

6.1 Conclusion

The main objective of the thesis is to implement a novel, compact size, omnidirectional, high efficiency DVB-H antenna to be used in the spectrum underlay cognitive radio (CR) systems, using metamaterial concept.

First, a survey on different techniques used to implement CR antennas was conducted in Chapter 2. As spectrum underlay CR system is chosen, the specs of the required antenna has been identified as: DVB-H, compact size, omnidirectional radiation pattern and high efficiency.

Metamaterial concept was chosen in order to meet the compact size requirements. A fundamental background was provided in Chapter 3. The possibility to achieve wideband operation by loading resonant type antennas with CRLH unit cells was explored. A printed-IFA was designed, fabricated and measured. Although wideband operation could not been achieved using this

approach, the results were interesting enough to be accepted for publication in IEEE Antennas and Wireless Propagation Letters.

Metamaterial inspired electrically small antennas (ESAs) is another approach of using metamaterial concept to achieve compact size requirement. A survey on the progress done in this approach is conducted in Chapter 4.

Lastly, as metamaterial inspired ESA provides a method to achieve size reduction, a model was proposed in chapter 5 to add the wideband operation feature. An electrically small DVB-H antenna was designed, fabricated and measured.

6.2 Future Work

The work presented in this thesis can be used in future work as follows:

1 This work can be extended to implement a spectrum interweave CR system. As the proposed DVB-H antenna represents a compact size sensing antenna, reconfigurable antenna can be implemented using any of the approaches stated in Chapter 2.

2 The model proposed in Chapter 5 describes exactly how the bandwidth of the antenna can be controlled using lumped elements. It also serves as a map for the frequencies supported by certain host antenna. Thus, wideband/multiband operation can be easily designed.

3 A further extension to the proposed model is to design the antenna based on a given lumped element network parameters.

6.3 List of Publications

Accepted papers

A. Raslan, A. Ibrahim and A. Safwat, "Resonant-Type Antennas Loaded With CRLH Unit Cell," *IEEE Antennas and Wireless Propagation Letters,* vol. 12, pp. 23-26, 2013.

Papers in the Reviewing Process

A. Raslan, A. Safwat, " N-Internal Port Design for Wide Band Electrically Small Antennas with Application for UHF Band," submitted to *IEEE Transactions on Antennas and Propagation,* Apr. 2013.

References

[1] http://web.it.kth.se/~maguire/jmitola/Mitola_Dissertation8_Integrated.pdf, " [Online].

[2] "http://transition.fcc.gov/pshs/techtopics/techtopic8.html," [Online].

[3] Y. Tawk, M. Bkassiny, G. El-Howayek, S. Jayaweera, K. Avery and C. Christodoulou, "Reconfigurable front-end antennas for cognitive radio applications," *IET Microwaves, Antennas & Propagation*, vol. 5, no. 8, pp. 985-992, 2011.

[4] M. Al-Husseini, K. Kabalan, A. El-Hajj and C. Christodoulou, "Cognitive Radio: UWB Integration and Related Antenna Design", InTech, 2010.

[5] Y. Tawk, J. Costantine, K. Avery and C. Christodoulou, "Implementation of a Cognitive Radio Front-End Using Rotatable Controlled Reconfigurable Antennas," *IEEE Transactions on Antennas and Propagation*, vol. 59, no. 5, pp. 1773-1778, May. 2011.

[6] M. Al-Husseini, Y. Tawk, C. Christodoulou, K. Kabalan and A. El-Hajj, "A reconfigurable cognitive radio antenna design," *Antennas and Propagation Society International Symposium (APSURSI)*, Toronto, ON, 2010.

[7] E. Erfani, J. Nourinia, C. Ghobadi, M. Niroo-Jazi and T. Denidni, "Design and Implementation of an Integrated UWB/Reconfigurable-Slot Antenna for Cognitive Radio Applications," *IEEE Antennas and Wireless Propagation Letters*, vol. 11, pp. 77-80, 2012.

[8] Y. Tawk, S. Jayaweera, C. Christodoulou and J. Costantine, "A comparison between different cognitive radio antenna systems," *International Symposium on Intelligent Signal Processing and Communications Systems (ISPACS)*, pp.1-5, Chiang Mai, 2011.

[9] "DVB-H implementation guidelines," *European Telecommunication Std., Rev. TR 102 377 V1.4.1*, April 2009.

[10] L. Huitema, T. Reveyrand, E. Arnaud, C. Decroze and T. Monediere, "A compact and reconfigurable DVB-H antenna for mobile handheld devices," *Proceedings of the 5th European Conference on Antennas and Propagation (EUCAP)*, 2011.

[11] F. Canneva, J. M. Ribero and R. Staraj, "Reconfigurable meander antenna for DVB-H band," *International Workshop on Antenna Technology (iWAT)*, Lisbon ,2010.

[12] F. Canneva, F. Ferrero, J.-M. Ribero and R. Staraj, "Reconfigurable miniature antenna for DVB-H standard," in *IEEE Antennas and Propagation Society International Symposium (APSURSI)*, 2010.

[13] C. Sanchez, J. De Mingo, P. Garcia, P. Carro and A. Valdovinos, "Application of an Impedance Tuning Network for Mobile DVB-H Terminals," in *Vehicular Technology Conference Fall (VTC 2009-Fall), 2009 IEEE 70th*, 2009.

[14] S.S. Zhong, "UWB and SWB Planar Antenna Technology," in *Microwave and Millimeter Wave Technologies Modern UWB antennas and equipment*, InTech, 2010.

[15] V. Rumsey, "Frequency independent antennas," in *IRE International Convention Record*, vol.5, pp. 114 – 118, 1957.

[16] X. F. Bai, S. S. Zhong and X. L. Liang, "Leaf-shaped monopole antenna with extremely wide bandwidth," *Microwave and Optical Technology Letters*, vol. 48, no. 7, pp. 1247-1250, 2006.

[17] X. Liang, S. Zhong and W. Wang, "Elliptical planar monopole antenna with extremely wide bandwidth," *Electronics Letters*, vol. 42, no. 8, pp. 441-442, Apr. 2006.

[18] X. Liang, S. Zhong, W. Wang and F. Yao, "Printed annular monopole antenna for ultra-wideband applications," *Electronics Letters*, vol. 42, no. 2, pp. 71-72, Jan. 2006.

[19] J. Zhao, T. Peng, C.-C. Chen and J. Volakis, "Low-profile ultra-wideband inverted-hat monopole antenna for 50 MHz-2 GHz operation," *Electronics Letters*, vol. 45, no. 3, pp. 142-144, 2009.

[20] Y.W. Chi, K.-L. Wong and S.-W. Su, "Broadband Printed Dipole Antenna With a Step-Shaped Feed Gap for DTV Signal Reception," *IEEE Transactions on Antennas and Propagation*, vol. 55, no. 11, pp. 3353-3356, 2007.

[21] S.-L. Zuo, Z.-Y. Zhang and J.-W. Yang, "Planar Meander Monopole Antenna With Parasitic Strips and Sleeve Feed for DVB-H/LTE/GSM850/900 Operation in the Mobile Phone," *IEEE Antennas and Wireless Propagation Letters*, vol. 12, pp. 27-30, 2013.

[22] J. Pendry, A. J. Holden, D. J. Robbins and J. Stewart, "Magnetism from conductors and enhanced nonlinear phenomena," *IEEE Transactions on Microwave Theory and Techniques,* vol. 47, no. 11, pp. 2075-2084, 1999.

[23] C. Caloz and T. Itoh, Electromagnetic Metamaterials: Transmission Line Theory and Microwave Applications, 1 ed., Wiley IEEE Press, 2005.

[24] V. Veselago, "The electrodynamics of substances with simultaneously negative values of ε and μ," *Soviet Physics Uspekhi,* vol. 10, no. 4, p. 509–514, Jan., Feb. 1968.

[25] R. A. Shelby, D. R. Smith and S. Schultz, "Experimental Verification of a Negative Index of Refraction," *Science,* vol. 292, no. 5514, pp. 77-79, Apr. 2001.

[26] J. B. Pendry, A. J. Holden, D. J. Robbins and W. J. Stewart, "Low frequency plasmons in thin-wire structures," *Journal of Physics: Condensed Matter,* vol. 10, no. 22, p. 4785, Jun. 1998.

[27] D. M. Pozar, Microwave Engineering, 3 ed., Wiley, 2004.

[28] H. V. Nguyen, "Novel broadband conventional- and dual-composite right/left-handed (C/D-CRLH) metamaterials: properties, implementation and double-band coupler application," vol. 87, no. 2, pp. 309-316, 2007.

[29] A. Rennings, S. Otto, J. Mosig, C. Caloz and I. Wolff, "Extended composite right/left-handed (E-CRLH) metamaterial and its application as quadband quarter-wavelength transmission line," in *Asia-Pacific Microwave Conference (APMC),* pp. 1405 - 1408, Yokohama, 2006.

[30] Ibrahim, A. M. E. Safwat and H. El-Hennawy, "Triple-Band Microstrip-Fed Monopole Antenna Loaded With{CRLH Unit Cell," *IEEE Antennas and Wireless Propagation Letters,* vol. 10, pp. 1547-1550, 2011.

[31] Ibrahim and A. M. E. Safwat, "Microstrip-Fed Monopole Antennas Loaded With CRLH Unit Cells," *IEEE Transactions on Antennas and Propagation,* vol. 60, no. 9, pp. 4027-4036, 2012.

[32] A. Balanis, Antenna Theory: Analysis and Design, 3rd Edition, 3rd ed., Wiley Interscience, 2005.

[33] K. L. Wong, Planar Antennas for Wireless Communications, Wiley-Interscience, 2003.

[34] M. Ammann and M. John, "Optimum design of the printed strip monopole," *IEEE Antennas and Propagation Magazine,* vol. 47, no. 6, pp. 59-61, 2005.

[35] H. Wheeler, "The Radiansphere around a Small Antenna," *Proceedings of the IRE,* vol. 47, no. 8, pp. 1325-1331, 1959.

[36] W. McKinzie, "A modified Wheeler cap method for measuring antenna efficiency," *IEEE Antennas and Propagation Society International Symposium*, vol. 1, pp. 542 – 545, 1997.

[37] R. Johnston and J. McRory, "An improved small antenna radiation-efficiency measurement method," *IEEE Antennas and Propagation Magazine,* vol. 40, no. 5, pp. 40-48, 1998.

[38] M. Geissler, O. Litschke, D. Heberling, P. Waldow and I. Wolff, "An improved method for measuring the radiation efficiency of mobile

devices," *IEEE Antennas and Propagation Society International Symposium*, vol. 4, pp. 743 – 746, Columbus, OH, 2003.

[39] ARRL Antenna Book 22nd Edition, Antennas, Transmission Lines and Radio Wave Propagation, 2011.

[40] J. F. Zürcher, I. Giangrandi, O. Staub and A. K. Skrivervik, "A dual-frequency printed conformable antenna for mobile communications," *Microwave and Optical Technology Letters,* vol. 27, p. 386–390, Dec. 2000.

[41] H. Wheeler, "Fundamental limitations of small antennas," *Proceedings of the IRE,* vol. 35, no. 12, pp. 1479-1484, Dec. 1947.

[42] R. Ziolkowski and A. Erentok, "Metamaterial-based efficient electrically small antennas," *IEEE Transactions on Antennas and Propagation,* vol. 54, no. 7, pp. 2113-2130, Jul. 2006.

[43] R. W. Ziolkowski and A. D. Kipple, "Application of Double Negative Materials to Increase the Power Radiated by Electrically Small Antennas," *IEEE Transactions on Antennas and Propagation,* vol. 51, no. 10, Oct. 2003.

[44] A. Erentok and R. Ziolkowski, "A Hybrid Optimization Method to Analyze Metamaterial-Based Electrically Small Antennas," *IEEE Transactions on Antennas and Propagatio,* vol. 55, no. 3, pp. 731-741, Mar. 2007.

[45] A. Erentok and R. Ziolkowski, "Metamaterial-Inspired Efficient Electrically Small Antennas," *IEEE Transactions on Antennas and Propagation,* vol. 56, no. 3, pp. 691-707, Mar. 2008.

[46] C. C. Lin, P. Jin and R. Ziolkowski, "Multi-Functional, Magnetically-Coupled, Electrically Small, Near-Field Resonant Parasitic Wire Antennas," *IEEE Transactions on Antennas and Propagation,* vol. 59, no. 3, pp. 714-724, Mar. 2011.

[47] R. Ziolkowski, "Efficient Electrically Small Antenna Facilitated by a Near-Field Resonant Parasitic," *Antennas and Wireless Propagation Letters, IEEE,* vol. 7, pp. 581-584, 2008.

[48] P. Jin and R. Ziolkowski, "Low-Q, Electrically Small, Efficient Near-Field Resonant Parasitic Antennas," *IEEE Transactions on Antennas and Propagation,* vol. 57, no. 9, pp. 2548-2563, Sep. 2009.

[49] P. Jin and R. Ziolkowski, "Multi-Frequency, Linear and Circular Polarized, Metamaterial-Inspired, Near-Field Resonant Parasitic Antennas," *IEEE Transactions on Antennas and Propagation,* vol. 59, no. 5, pp. 1446-1459, May 2011.

[50] C. C. Lin, P. Jin and R. Ziolkowski, "Single, Dual and Tri-Band-Notched Ultrawideband (UWB) Antennas Using Capacitively Loaded Loop (CLL) Resonators," *IEEE Transactions on Antennas and Propagation,* vol. 60, no. 1, pp. 102-109, Jan. 2012.

[51] N. Zhu, R. Ziolkowski and H. Xin, "Electrically Small GPS L1 Rectennas," *Antennas and Wireless Propagation Letters, IEEE,* vol. 10, pp. 935-938, 2011.

[52] J. T. Aberle and R. Lopesinger-Romak, Antenna With Non-Foster, San Rafael, CA: Morgan & Claypool Pub-lishers, 2007.

[53] P. Jin and R. Ziolkowski, "Broadband, Efficient, Electrically Small Metamaterial-Inspired Antennas Facilitated by Active Near-Field Resonant Parasitic Elements," *IEEE Transactions on Antennas and Propagation,* vol. 58, no. 2, pp. 318-327, Feb. 2010.

[54] N. Zhu and R. Ziolkowski, "Active Metamaterial-Inspired Broad-Bandwidth, Efficient, Electrically Small Antennas," *Antennas and Wireless Propagation Letters, IEEE,* vol. 10, pp. 1582-1585, 2011.

[55] P. Jin and R. Ziolkowski, "Metamaterial-Inspired, Electrically Small Huygens Sources," *Antennas and Wireless Propagation Letters, IEEE,* vol. 9, pp. 501-505, 2010.

[56] M. Othman, T. Abuelfadl and A. Safwat, "Dual and Wide-Band Inductively-Loaded Dipole-Based Antennas for WLAN/UMTS Applications," *IEEE Transactions on Antennas and Propagation,* vol. 61, no. 3, pp. 1430-1435, 2013.

[57] "www.ansys.com," [Online].

[58] "www.coilcraft.com/misc/0603csd.html," [Online].

[59] H. A. Priestley, Introduction to Complex Analysis, Second Edition ed., Oxford University Press, 2003.

[60] "www.mathworks.com/products/matlab," [Online].

[61] R. E. Collin, Antennas and radiowave propagation, McGraw-Hill, 1985.

[62] L. J. Chu, "Physical limitations of omnidirectional antennas," 1948.